

Atomic-Precision Tailoring of Au-Ag Core-shell Composite Nanoparticles for Direct Electrochemical-Plasmonic Hydrogen Evolution in Water Splitting

*Jiaying Mo, Eduardo C.M. Barbosa, Simson Wu, Yiyang Li, Yuancheng Sun, Weikai Xiang, Tong Li, Shengda Pu, Alex Robertson, Tai-sing Wu, Yun-liang Soo, Tiago V. Alves, Pedro H.C. Camargo, Winson Kuo, and Shik Chi Edman Tsang**

J. Mo, Dr. E. C. M. Barbosa, Dr. S. Wu, Y. Li, Y. Sun, Prof. S.C.E. Tsang
The Wolfson Catalysis Centre, Department of Chemistry, University of Oxford, Oxford, OX1 3QR, UK
E-mail: edman.tsang@chem.ox.ac.uk

Dr. E. C. M. Barbosa, Prof. P. H. C. Camargo
Departamento de Quimica Fundamental, Instituto de Quimica, Universidade de Sao Paulo, Sao Paulo, SP, Brazil

W. Xiang, Prof. T. Li.
Institute for Materials, Ruhr Universität Bochum, Universitätsstr. 150, 44801 Bochum, Germany

S. Pu, Dr. A. Robertson.
Department of Materials, University of Oxford, Oxford, OX1 3PH, UK

Dr. T.-S. Wu, Prof. Y.-L. Soo
National Synchrotron Radiation Research Center, Hsinchu, Taiwan and Department of Physics, National Tsing Hua University, Hsinchu, Taiwan

Prof. T. V. Alves
Departamento de Físico-Química, Instituto de Química, Universidade Federal da Bahia Rua Barão de Jeremoabo, 147, 40170-115, Salvador, BA, Brazil

Prof. P. H. C. Camargo
Department of Chemistry, University of Helsinki, A.I. Virtasen aukio 1, Helsinki, Finland

Dr. W. Kuo
Materials Characterization Facility, Texas A&M University, 3471 TAMU, College Station, TX 77843, USA

Keywords: electrochemical, localized surface plasmon resonance, core-shell design, hydrogen evolution

Abstract: Traditionally bandgap materials are prerequisite to photocatalysis and electrochemical-photolysis due to their ability to harness a reasonable range of solar spectrum. However, the inevitable high impedance across the bandgap and the low concentration of intrinsic charge carriers have limited their energy conversion. By contrast, metallic nanoparticles possess sea of free electrons that can effectively promote transition to excited state for reaction. Here, an atomic layer of bimetallic concoction of silver-gold shell is precisely fabricated onto an Au core via a sonochemical dispersion approach to form a core-shell of Au-Ag that exploits the wide availability of excited states of Ag while maintaining an efficient local surface plasmon resonance (LSPR) of Au. Catalytic results demonstrate that this mix of Ag and Au can convert solar energy to hydrogen at high efficiency with an increase of 112.5% at an optimized potential of -0.5 V when compared to light-off conditions under the electrochemical-localized surface plasmon resonance. This outperforms the commercial Pt catalysts by 62.1% with a hydrogen production rate of $1870 \mu\text{mol g}^{-1}\text{h}^{-1}$ at room temperature. This study opens a new route for tuning the range of light capture of HER catalysts using fabricated core-shell material through the combination of LSPR with electrochemical means.

1. Introduction

Hydrogen is well accepted as one of the cleanest chemical vectors for sustainable storage of solar energy.^[1–5] The landmark report by Fujishima and Honda et al.^[6] in 1970s demonstrates the feasibility to carry out photocatalytic or photoelectrochemical (PEC) splitting of water into H₂ and O₂ by using semiconductor TiO₂ electrode. Semiconductor-based nanomaterials are generally considered as promising candidates in converting solar energy into clean and carbon-neutral H₂ fuel due to their efficient formation of electron-hole pairs and charge separation and migration.^[7–9] It is thus possible to relay on tuning of semiconductor materials to capture a specific range of solar spectrum for a series of photo-processes but the inevitable high impedance across the bandgap and the low concentration of intrinsic charge carriers have concomitantly limited their energy conversion causing a low solar-to-hydrogen (STH) efficiency.^[10–12] In addition, the high cost of rare metals such as platinum as catalyst to promote the semiconductors for such hydrogen production should be noted.

By contrast, the use of metal nanoparticles (NPs) with higher electron density and mobile conductive electrons will not lead to significant impedance as that of semiconductor. Some metals (e. g., Ag or Au) give outstanding conductivity and optical properties in the visible and/or near infrared ranges. The oscillation of free conduction electrons on these metallic NPs relative to the static nuclei in response to an oscillating electric field from an incoming electromagnetic wave accounts for the strong localized surface plasmon resonance (LSPR) excitation.^[13] Importantly, the plasmonic resonance is narrowly concentrated around the plasmon peak in light energy capture (energy confinement) and can also generate high-energy non-thermal hot electrons (HEs) in the NPs. The HE generation is predominantly a quantum process driven by optical electric field hot spots and surface-assisted scattering.^[14] However, direct use of these LSPR-generated HEs in photocatalytic HER without the use of bandgap materials under visible light illumination has rarely been reported yet, presumably due to the lack of appropriate design of catalytic system.

Notice that it has been recently established that the LSPR excitation in plasmonic metal nanoparticles can be indirectly used to assist semiconductor in photocatalysis, which can act as both light absorbers and electron mediators, enabling to lower recombination rates when combined with semiconducting materials.^[13,15–17] However, the high work functions of the plasmonic metal NPs (e.g., Au or Ag NPs) make it quite challenging for the LSPR-excited electrons to reach to the energy level for proton reduction from water without the help of the bandgap materials. On the other hand, there is an exciting possibility to develop an integrated system that couples LSPR excitation with electrical potential from renewable energy sources for electrochemical water reduction.^[18–22] Pang and co-workers have demonstrated the use of Au/Ti/TiO₂ adhesion layer for efficient LSPR-excited hot electron injection from Au thin layer into the underlying TiO₂-based layer so as to decrease the activation energy for HER.^[18] Meanwhile, Shi et.al. reported the use of plasmonic Au-MoS₂ hybrid to greatly improve the HER by increasing the carrier density in MoS₂ induced by the injection of hot electrons from Au nanorods.^[19] However, most of the reported methods rely on semiconductors to act as electron acceptors for hydrogen production so as to inject LSPR-excited hot electrons to the conduction band, in turn limiting charge transfer and conductivity due to the nature of these bandgap materials. As a result, the direct contribution of electrochemical-localized surface plasmon resonance (EC-LSPR) capture of visible light for hydrogen production from water over metallic nanoparticles on polarized electrode without the use of bandgap materials was evaluated in this work. It is anticipated that such direct harness of solar energy by plasmonic HEs for hydrogen formation from water on electric polarized metallic surface may offer a new mean in photocatalysis.

Herein our study, we have employed bifunctional bimetallic Au-Ag/Au core-shell catalysts where the role of silver is for the provision of higher energy (more positive) excited states as an avenue to allow LSPR-promoted hot electrons to carry out proton reduction whereas the role of gold is for plasmonic absorption to capture major solar radiations. Au and Ag are

strategically adopted as the active metal centre due to their possession of high molar extinction coefficient, sharp resonance and excellent performance in electrochemical reactions among all metals.^[23–25] Moreover, the peak absorption wavelength can easily be tuned by adjusting the composition, geometry and support (variation in dielectric constants) of the Au-Ag bimetallic nanoparticle.^[26–28] To maximize atomic efficiency, a multitude of surface modification methods^[29,30] such as geometric dimension control have been proposed to achieve atomic structure. In this study, novel hetero-nanostructured core-shell type material with a tunable mixed-shell composition and shell thickness (down to atomic level), christened as atomic (AT)-layer, intermediate (IN)-layer and thick (TH)-layer, are successfully prepared by gradual reduction process. We have successfully fabricated an atomic layer of optimally-balanced silver-gold mixture precisely onto an Au core via a sonochemical dispersion approach. It is demonstrated that the AT-layer of 20% Ag-80% Au offers an excitingly 112.5 % current enhancement in the presence of visible light during electrolysis, giving a hydrogen production rate of $1870 \mu\text{mol g}^{-1}\text{h}^{-1}$ at room temperature, which is 10 times higher than most semiconductor catalyst system under similar reaction conditions (Table S1-S3).^[31–37] By using an energy dispersive X-ray spectroscopy (EDX) in conjunction with atom probe tomography (APT) coupled with discrete dipole approximation (DDA) calculations, we have shown a significant amplification of the plasmonic electric field in the near-shell region, giving rise to a maximum optical absorption. We believe that this work represents an excellent means in engineering nano-architecture, in particular tunable core-shell materials, which may provide a more economic and efficient alternative to the electrolysis over commercial Pt catalysts in the new EC-LSPR system. The ultimate aim is therefore to develop a protocol that can maximize the use of LSPR to capture solar energy in order to reduce the use of energy-intensive bias potential.

2. Results and Discussions

2.1. Structural and compositional characterizations

The fabrication process of the three Au-Ag core-shell catalysts are schematically illustrated in **Figure 1a** and described in detail in the Supporting Information. Briefly, Ag layers was selectively grown on the preformed Au cores by stepwise Ag reduction to form the core-shell Au-Ag NPs,^[38] accompanying an obvious colour change from wine red to orange. Both pure Ag and Au NPs (except TH-layer where pure Ag NPs can be identified) were not found in the core-shell samples as carefully examined by TEM, suggesting the highly selective growth of Ag on the Au cores. The pure Au and Ag nanoparticles were also synthesized as reference materials and were characterized by transmission electron microscopy (TEM, Supporting Information Figure S1-S2), yielding a mean diameter of 26.6 nm for the Au core and 24.9 nm for the Ag NPs.

It is becoming clear that the quality factor of the plasmonic resonance is critically dependent on the chemical composition and interfacial structure of NPs.^[39,40] Although in the bulk form, Ag and Au are mutually soluble in all compositions according to phase diagram.^[39] the behavior of the bulk materials with regard to miscibility or phase stability is a poor guide to interfacial nanoscale structures. It is however, very challenging to characterize NP materials' interface in the composite Au-Ag core-shell even by the help of high resolution TEM imaging. As a result, high resolution super EDX was particularly employed to obtain elemental mapping of the core-shell structures. The super EDX analysis clearly indicated that the increasing thickness of Ag rich shell boundary from atomic layer on Au core when the Ag content is increased (Figure 1b-d).

However, the two-dimensional projected Ag and Au signals of the core-shell nanoparticle make it difficult to differentiate their precise locations. Atom probe tomography (APT) can provide uniquely powerful atomic-scale mapping of nanoparticles in three-dimensions. Thus, APT was employed to analyze the elemental concentration in the shell and core. Slices shown

in Figure 1h-j were taken from the 3D APT reconstructions Figure 2e-g through each particle for atomic depth profiling. The mean interfacial regions in the shells of AT-layer, IN-layer and TH-layer of Au-Ag core-shell nanoparticles were determined to be 0.5 (shell thickness = 1.1 nm), 2.1 (shell thickness = 2.7 nm) and 2.7 (shell thickness = 5.4 nm) nm, respectively within ± 0.6 nm errors (Figure 1k-m and Figure S3-S5). APT reveals their concentration profiles at the interface regions of the core-shell heterostructures varying from almost pure Ag (except the AT-layer) at outermost layer to pure Au core in Figure 1k-m. For the AT-layer case, although the shell thickness is in about the dimension of atomic thickness, there is no pure Ag atomic shell but still a mixture of Ag and Au atoms on Au core. The average compositions of the interfaces in AT-layer, IN-layer and TH-layer Au-Ag core-shell are determined to be “20% Ag and 80% Au”, “40% Ag and 60% Au” and 50% Ag and 50% Au”, respectively.

As a result, there is no clear ordered segregation of Ag atoms in any local region but both Au and Ag atoms clearly have diffused across the material boundaries to give the atomically disordered and unblunt interfaces, reinforcing their excellent mutual atomic miscibility. This leads to a gradual mixing of Au and Ag atoms at the interfacial regions as also evidenced by both super EDX and APT analyses. The resultant compositions are also in good agreement with the synthesis ratio when the self-nucleation and trace size variation are taken into account.

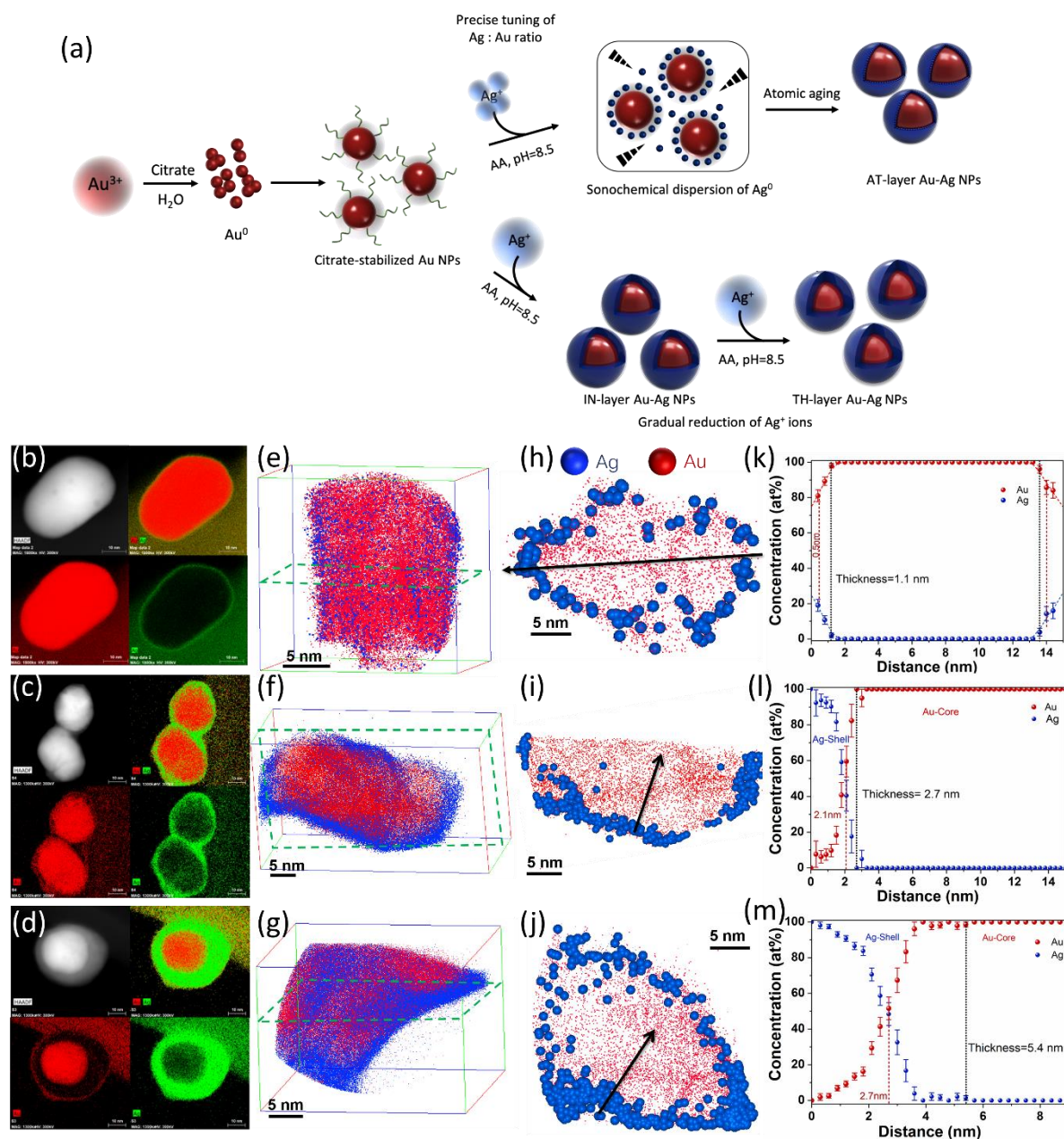


Figure 1. Schematic synthetic process and structural characterizations. a) Schematic illustration of sonochemical dispersion and gradual reduction process used to synthesize the Au-Ag core-shell nanoparticles. b, c, d) HAADF-STEM images and corresponding super EDX spectrum for individual (b) AT-layer Au-Ag, (c) IN-layer Au-Ag and (d) TH-layer Au-Ag nanoparticles showing the elemental mapping of the core and shell. Au (red), Ag (green). e, f, g) 3D APT reconstruction of AT-layer Au-Ag, IN-layer Au-Ag and TH-layer Au-Ag nanoparticles. h, i, j) Cross-sectional atom map as indicated by the dotted box in the 3D APT reconstruction diagram. k, l, m) 1D concentration profile of Ag and Au across the line from shell to core based on the arrow in the cross-sectional atom maps in (h), (i) and (j). Au (red), Ag (blue).

2.2. Surface plasmon analysis

Interestingly, the as-prepared Au and Ag NPs exhibit strong plasmonic absorption but well separated peak at the peak maxima at 532 nm and 400 nm, respectively in the visible light regime (**Figure 2a**). As a result, it follows logically that the optical properties of the core-shell Au-Ag NPs lie between the two plasmon resonance frequencies of Ag and Au. From Figure 2a, it can be observed that the peak position of the UV-Vis spectrum of the AT-layer Au-Ag core-shell is similar to that of Au core with a clear blue shift to 528 nm. Thus, the position of the LPSR adsorption peak can even be sensitized by the single atomic alloy layer (20% Ag and 80% Au) on Au core as shown by the Super-EDX and APT. When the shell thickness increases to 2.7 nm, the plasmon resonance is attenuated and the peak blue-shifted further to 509 nm with a new extinction peak appears at 370 nm. The latter peak can clearly be attributed to the outermost primarily Ag shell with the similar absorption to pure Ag but the alloy interfacial regions (40% Ag and 60% Au) on Au core shown by 509 nm peak can also exert their effect to the absorption. When the shell thickness reaches 5.4 nm, Ag outer shell absorption becomes dominant with the major absorption peak shifted to 386 nm but the strongly shifted Au (~500 nm) can only be visible as a small shoulder. Within experimental errors and materials variations, as a general observation, the plasmon resonance of the Au core nanosphere thus appears to be strongly masked or attenuated by that of the shell, and the Ag/Au alloyed shell resonances dominate.

The electromagnetic confinement enhancement in LSPR is particularly strong at the so-called “hot spots”, where the non-thermal “hot electron” can be generated with typical sizes of only few nanometers, which are usually located at the surface/edge of the composite nanoparticle.^[13,41–45] As a result, STEM/EELS is employed as a powerful tool to characterise the surface plasmons (LSPR-induced hot electrons) in sub-angstrom spatial resolution given its capability to excite the full set of LSPR modes.^[46,47] Particularly, Low-loss electron energy loss spectroscopy (EELS) of below 50 eV using a probe-corrected TEM at 200 keV was employed

to directly visualize the electromagnetic eigenmodes of surface plasmons in metallic nanoparticles.^[46,47] The spatial variations of localized surface plasmon resonance (LSPRs) due to differences in chemical composition of the composite core-shell NPs were revealed by line-scan EELS combined with HAADF-STEM imaging (high angle annular dark field scanning transmission electron microscope) to sub-nanometer spatial accuracy. HAADF-STEM images were taken across one particular core-shell nanoparticle and corresponding EELS of spectra were collected across 10 different positions on the nanoparticle starting from the vicinity of the NP to the edge of the shell and across to the gold core and back to the shell at the other end and finally back to the vicinity. It is also worth mentioning that following each acquisition recorded, the HAADF images we ensured that no visible beam damage (due to the inelastic scattering events) or carbon contamination had occurred.

Figure 2b shows an experimental dataset collected from an as-prepared AT-layer Au-Ag core-shell metallic nanoparticle. Pronounced changes were observed along the carefully pre-calibrated electron beam probe positions. As the beam position approaches the edge of the shell, the normalized intensity of a plasmonic EELS peak starts to grow gradually at the near edge (but without touching the edge surface) then grows to the maximum when it is positioned at the edge, depicting the radiative field strength from the particle surface. Within the tolerances of broad tails of zero-loss peak (ZLP), uneven thickness and low carbon contamination from the microscopic chamber, the EELS peak position is determined to be 2.34 eV which well corresponds to its UV-Vis absorption peak at 530 nm in Figure 2a (based on the Planck-Einstein equation^[48]). Despite the fact that peak intensity depends on sample thickness and variation in beam current density, the intensity of the peak greatly diminishes at the core of the particle and increases again when it gets to the edge of the particle at the other end with the same plasmon energy at 2.34 eV, giving to a double hump pattern. This is consistent with the fact that a plasmon manifests itself as a collective dynamic oscillation of charges accumulated mainly at the surfaces.^[39]

The same STEM-EELS treatment is also performed on the TH-layer Au-Ag core-shell NPs (Figure 2c) containing higher Ag shell content as a comparison where the plasmon energy peaks is found to be at 3.29 eV at the edge of the particles that again corresponds to the observed absorption peak for UV-Vis of corresponding composite NPs. STEM-EELS analysis of pure Au and Ag NPs were also performed for comparison (Figure S6-S7). Remarkably, when the maximum peak intensity of these samples are compared at the edge of the NP (less dependence on sample thickness), the AT-layer Au-Ag core-shell NP (arbitrary unit of 410) is significantly higher than that of the TH-layer of arbitrary unit of 206, Ag NP (at 3.17 eV with arbitrary intensity unit of 203) and Au NP (at 2.36 eV with arbitrary intensity unit of 130) (Figure 2d and Figure S6-S7), which again suggests that the electromagnetic enhancement at “hot spots” from the material surface clearly dependent on chemical composition. The mixed Ag and Au atoms in AT-layer gives the strongest EELS peak intensity presumably generating the most non-thermal HEs. Coincidentally, Sykes et al. recently reported that silver nanocube on gold substrate produces large concentration of non-thermal HEs from gold plasmonic absorption, which arises from anisotropic electron–electron scattering within sp-bands near Fermi surface.^[44]

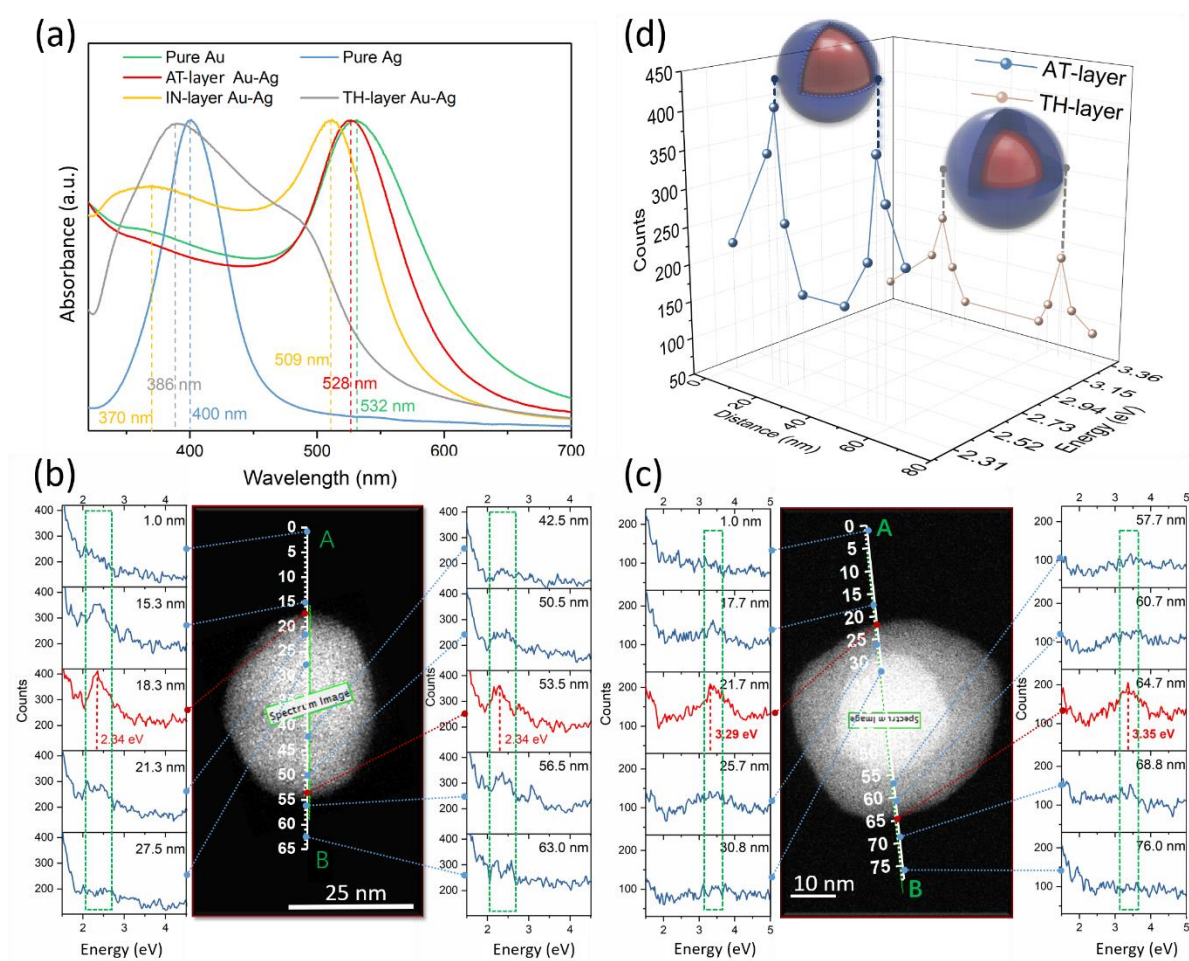


Figure 2. Surface plasmon analysis of the as-prepared samples. a) The normalized UV-Vis absorption spectra of pure Au, pure Ag and different Ag shell thickness of the Au-Ag core-shell NPs. b,c) A series of 10 successive low-loss STEM-EEL spectra acquired of a single (b) AT-layer Au-Ag core-shell nanoparticle and (c) TH-layer Au-Ag core-shell nanoparticle, in the spectrum-image mode, along an axis (A to B) of the nanosphere as illustrated in the inset. The position of the main resonance detected along the line scan are marked by dotted lines. d) Comparison of the plasmonic energy intensity between AT-layer and TH-layer core-shell NPs as a function of the electron probe position (intensity map) at 2.34 eV and 3.29 eV, respectively.

2.3. Direct Electrochemical-localized surface plasmon resonance (EC-LSPR)

In order to evaluate the electrochemical-localized surface plasmon resonance (EC-LSPR) efficiency of Ag-Au core-shell NPs variation of electrochemical potentials is applied with UV-cut Tungsten white light which mimics the solar spectrum.^[39,49] A three-electrode system was used to evaluate the electrocatalytic HER activities of the Au-Ag NPs in 0.5 M Na₂SO₄ electrolyte without any addition of sacrificial reagents under visible light illuminations (Figure S8). All the samples were dropped casted on the fluorine-doped tin oxide (FTO) glass and

evaluated at a bias potential of -0.3 V, -0.5 V, -0.8 V and -1.2 V versus Ag/AgCl (sat. KCl) reference electrode (Pt wire as counter electrode). **Figure 3a** demonstrates the envisaged energy diagram of water splitting process with references to standard reduction potential of proton to hydrogen and Au electrode (Fermi level of -5.11 eV from pure Au particle and -4.25 eV from pure Ag particle versus vacuum level, respectively^[50]). The values of Fermi level of pure Au and pure Ag in electron volts were converted to electrochemical energy potentials in volts according to the reference standard for which 0 V versus RHE (reversible hydrogen electrode) equals -4.44 eV versus evacuation (vacuum level).^[51–53] Although exact Fermi levels of our core-shell NPs are not yet known, and the pure Au and pure Ag values are only arbitrarily used. As seen from Figure 3a, the use of negative bias potential of 0.8 V or 1.2 V would reach above the energy threshold of hydrogen evolution reaction (HER) from electrolysis, which are thermodynamically sufficient to drive the reaction even without light irradiation; while in the case of -0.3 V and -0.5 V, the electrical energy itself cannot provide enough driving force for the hydrogen production.

Figure 3b shows the variation in hydrogen production rate (in form of current density) under visible light illumination from UV-cut Tungsten light ($\lambda > 420$ nm) for AT-layer Au-Ag core-shell NPs where the on-off cycles of photocurrent are stable and reproducible (Figure S9). A control experiment using carbon paper as the working electrode has been performed to preclude the possible role of FTO as semiconductor, which demonstrates similar change in current density at the light on/ off cycles (Figure S10). Figure S11 displays pure Au, pure Ag and the other two Au-Ag core-shell NPs for comparison. Notably, there is a significant enhancement in current density when visible light is illuminating on the catalyst surface (light on) at all bias potentials compared to light-off condition: such effect has not been previously recognized on metallic nanoparticles. A transient response of photocurrent with a current density of $1.68 \mu\text{A}/\text{cm}^2$ is also observed at 0 V applied bias potential from Figure S12 and Table S4, indicating that hot-electrons are generated under visible light illumination because of the

LSPR effect. As seen from the Figure 3b, the higher degree of polarization at stronger (more negative) bias potential clearly gives higher current density when light is on (Figure S13). This suggests that the LSPR effect that generates non-thermal HEs for protons reduction can be proportionally promoted in negative bias potential, presumably this charge separation process is fundamentally favoured. Recently, generation of plasmoelectric potential by plasmonic absorption to offer thermodynamic driving force to alter chemical potential of metallic particle is receiving intense attention.^[54] This looks like the reverse effect—the use of electric potential to increase plasmonic absorption from the metallic particle.

The gradual increase of the current density shown in Figure 3b, in contrast to the sharp rise as observed in semiconductors upon the light on, is attributed to the presence of Gouy-Chapman double charged layer around the catalyst surface in aqueous solution (Figure S14). Under visible light illumination, the photocatalytic hydrogen evolution reaction is readily promoted by the LSPR generated hot-electrons, which breaks the equilibrium between the metal surface charge and concentration of the solvated cation in the vicinity of the working electrode (in the diffuse layer). A “cooling-off” period is formed as a result during which cations in the outer layer diffuse through the solution and migrate towards the working electrode surface until a new equilibrium is reached. The transient decay of the photocurrent in the light off, on the other hand, is due to the release of the accumulated electrons generated during irradiation.^[55,56]

Among the measured samples, AT-layer Ag-Au NPs show the highest current density enhancement across the whole potential range from -0.3 V to -1.2 V (**Table 1**), giving an impressive overall hydrogen evolution rate of 1870 $\mu\text{mol g}^{-1}\text{h}^{-1}$ at -0.5 V under visible light illumination, matching with the EELS experiment due to the superiority of Ag-Au atomic surface on Au core. This LSPR promotion for HER from water by visible light is more favorable compared to electrolysis under the same potential range using expensive commercial Pt catalyst, especially exceeding the latter by 62.1% at -0.5 V (Figure S15 insert). Compared to light off experiments it can also be observed that the photocurrent intensity enhancement increases to

the maximum at -0.5 V and then decreases when the potential deviates from this bias value on both sides for all of our samples (as shown in Table 1). This volcano relationship is pertinent to the energy diagram shown in Figure 3a that the light energy capture contributes at lower extent to the proton reduction current either at too low negative bias potential (insufficient promotion energy) or too high over-potential that starts electrolysis.

From energy perspective, the optimum practice of this integrated process depends on cost and energy sources to generate the bias potential for efficient light capture. As a result, the LSPR of Au enables effective light energy capture at 530 nm where the oscillated electrons in the presence of Ag and Au mixed atoms on the AT-layer core-shell surface can also be promoted to non-thermal HEs for proton reduction. **The presence of surface Ag atoms in Au atom matrix on NP surface greatly facilitates the energy transfer for electron excitation which is consistent with the fact that the higher energy (more positive) and greater mobility of electrons are associated with Ag (Au gives higher ionization energy with higher effective nuclear charge than Ag because of lanthanide contraction and relativistic effect of 6 s electrons).**

To demonstrate the practical capability of EC-LSPR current enhancement for the AT-layer Au-Ag core-shell NPs, a solar simulator (AM 1.5G, 100 mW cm⁻²) equipped with an ultraviolet filter was also employed at an applied potential of -0.5 V. As seen from Figure 3d, the results indicate that the current enhancement under sunlight (110.8%) is similar to that under tungsten light (112.5%). LSPR current enhancement in different wavelength ranges at similar power density (selectively filtered from the solar spectrum) has also been studied. It is clearly demonstrated that the maximum enhancement (51.3%) is from the 500-600 nm region with an apparent quantum efficiency of 4% (Table S5), which is in good agreement with the UV-Vis plasmonic absorption peaks from AT-layer Au-Ag core-shell nanoparticles. It can be observed from Figure S16 that the trend of the spectra profile (in terms of apparent quantum efficiency) is matching with the absorption spectra of AT-layer nanoparticles in general. This sheds light on the fact that the hydrogen generated in the reaction is as a result of photocatalysis and hence,

the enhancement in the photocatalytic hydrogen evolution rate can be attributed to the plasmon resonance of the Au-Ag core-shell nanoparticles.

Additionally, the transient photocurrent response of AT-layer Au-Ag core-shell NPs was measured using continuously linear sweep voltammetry (LSV) under on/off visible light illumination. As we can see from Figure 3c, an obvious enhancement of photocurrent was obtained when the sample is under visible light illumination (whereas the current exhibits no change when light is off), which strongly implies that hot-electrons generated from LSPR effect of the core-shell NPs can greatly promote the hydrogen evolution reaction. The current density under visible light illumination is generally more negative than the light-off condition at the whole potential range (0 V-1.2 V vs Ag/AgCl). In other words, with the aid of LSPR generated hot-electrons under light illuminations, less electrical energy is required to promote the HER reaction, indicative the efficient conversion of light energy to hydrogen (Figure S15 and S17).

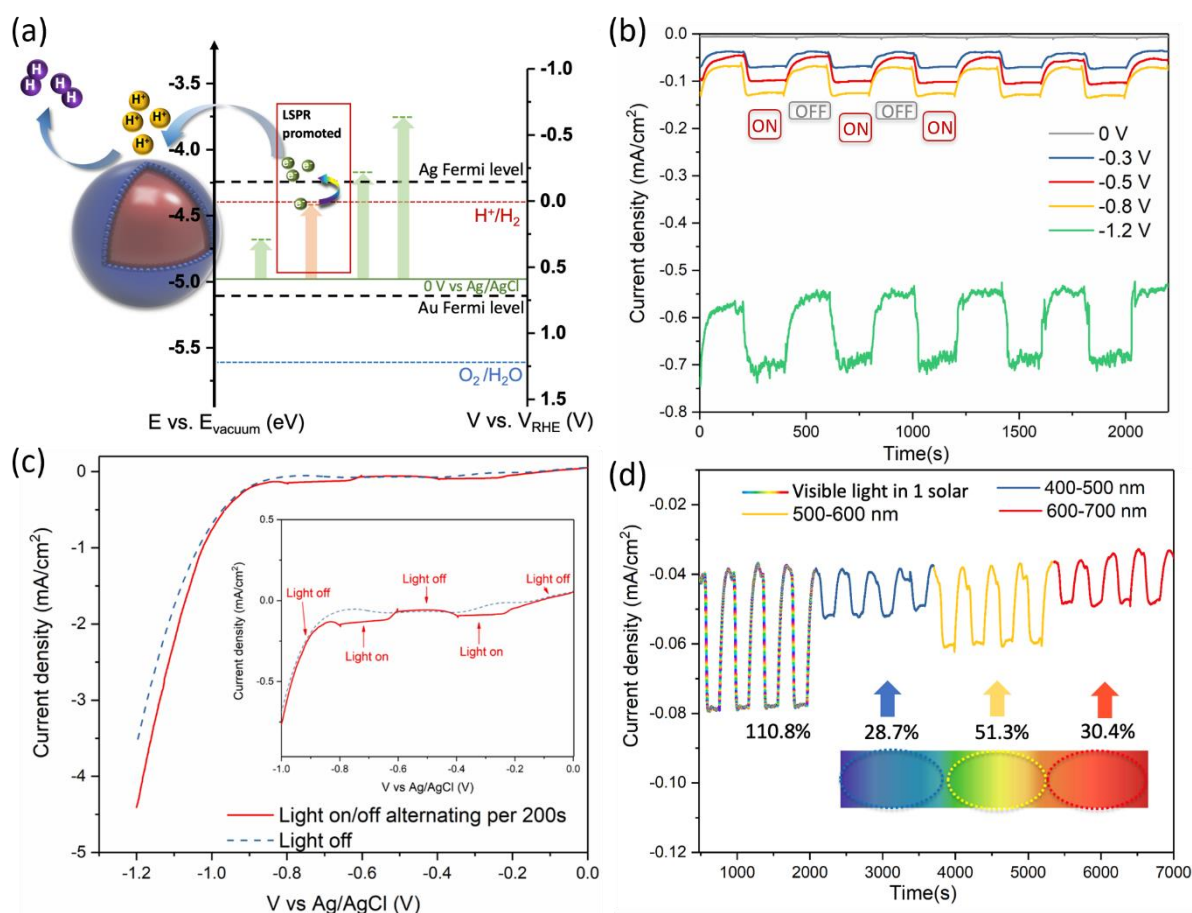


Figure 3. Catalytic performance of the as-prepared samples. a) Schematic illustration of energy diagram and hot electrons transfer mechanism using LSPR excitation on AT-layer Au-Ag core-shell NPs, green bars from left to right represent: -0.3 V, -0.8 V and -1.2 V versus Ag/AgCl while the red bar is -0.5 V versus Ag/AgCl. b) Current density as a function of reaction time of AT-layer Au-Ag NPs at 0 V, -0.3 V, -0.5 V, -0.8 V and -1.2 V versus Ag/AgCl under UV-cut ($\lambda > 420$ nm) tungsten light. c) Linear sweep voltammetry (LSV) curves and transient photocurrent densities of the AT-layer Au-Ag core-shell NPs in 0.5 M of Na_2SO_4 electrolyte under visible light illumination ($\lambda > 420$ nm) with 200 s light-on/off cycles. The scan rate is 1 mV/s. The insert image is the enlarge LSV curve in the range of 0 V-1.0 V versus Ag/AgCl. d) Current density as a function of reaction time of AT-layer Au-Ag NPs at -0.5 V versus Ag/AgCl under selected ranges of wavelengths of a solar simulator.

Table 1. The EC-LSPR current density enhancement of pure Au, pure Ag, AT-layer Au-Ag, IN-layer Au-Ag and TH-layer Au-Ag supported on Vulcan carbon (/C) at applied potentials of -0.3 V, -0.5 V, -0.8 V and -1.2 V, respectively under visible light illuminations ($\lambda > 420$ nm) compared with dark conditions.

Applied potentials	Au/C	AT-layer Au-Ag/C	IN-layer Au-Ag/C	TH-layer Au-Ag/C	Ag/C
-0.3 V	50.8%	82.1%	70.4%	59.8%	53.4%
-0.5 V	54.7%	112.5%	79.3%	62.7%	57.5%
-0.8 V	28.3%	76.8%	54.3%	53.2%	31.3%
-1.2 V	17.0%	26.1%	23.5%	21.3%	19.2%

2.4. X-ray absorption spectroscopy and discrete dipole approximation simulation

Obviously, the shell composition may also be altered with the shell thickness as evidenced by our APT measurements (Figure 1). As a result, X-ray absorption fine structure (EXAFS) of both Ag K-edge and Au L₃-edge have also been used to analyze the composition of Ag and Au by probing the coordination environment of the two metals. Fourier transformed chi functions of Ag K-edge are first used to disseminate the difference between the atomic layer and the other shell-thickness core-shell nanoparticles. As displayed in **Figure 4a**, the chi functions of IN-Layer and TH-layer resemble to that of the Ag foil while that of AT-layer shows a stark contrast in peak shapes and peak positions especially at the higher k values ($> 6 \text{ \AA}^{-1}$). Fitting with Ag-Ag and Ag-Au scattering paths suggest some heavier elements, in this case Au, are coordinating to Ag in the shell, which supports our argument in atomic probe tomography of an apparent Ag:Au interface (Figure 4b). Meanwhile, wavelet restorations have been implemented in order to spatially resolve the close bond distance between Au-Ag ($\sim 2.88 \text{ \AA}$) and Ag-Ag ($\sim 2.89 \text{ \AA}$). As observed in Figure 4c-e, the wavelet is clearly resolved into 2 different energy maxima at low k ($\sim 3.5 \text{ \AA}^{-1}$, assign to lighter element Ag) and high k ($\sim 8.2 \text{ \AA}^{-1}$, assign to heavier element Au) at approximately 2.5 \AA (2.9 \AA after phase transfer). As Figure 4d and 4e suggests, the lower energy maxima (Ag) in the wavelet of IN-layer and TH-layer are heavily biased towards the higher energy maxima, which suggests the bulk nature of Ag in the thicker shell nanoparticles. On the other hand, the wavelet for atomic layer is clearly resolved in two peaks which is stemmed from the distinct interaction of Ag-Au and Ag-Ag at the interface.

Least square fitting, with amplitude reduction factor obtained from Au (Figure S18) and Ag (Figure S19), further reveals the major contribution of the signal for the IN-layer and TH-layer sample comes from the Ag-Ag scattering path (CN ~ 11 with Ag-Au of 1CN), which is in stark contrast to the AT-layer sample that has only 2-coordination of Ag-Ag but ~ 6 -coordination of Ag-Au in the NP (**Table 2**, Figure S20-S22). Given the similar size of the gold

core and hence a similar surface area of Ag-Au interface, the results imply that some of the silver-gold interaction must be originated from the shell of mixed atoms. This is in good agreement with the APT results that shows a significant composition of mixed Ag-Au atoms in the AT-layer sample. Regarding the Au L₃ edge absorption (**Table 3**, Figure S23-S25), it also shows a descending order of Au-Ag coordination as the shell thickness increases. It is worthwhile to note the Au-Ag interaction in the AT-layer is comparatively smaller than that of the Ag K-edge since the majority of the signal is dominated by the gold core in this analysis.

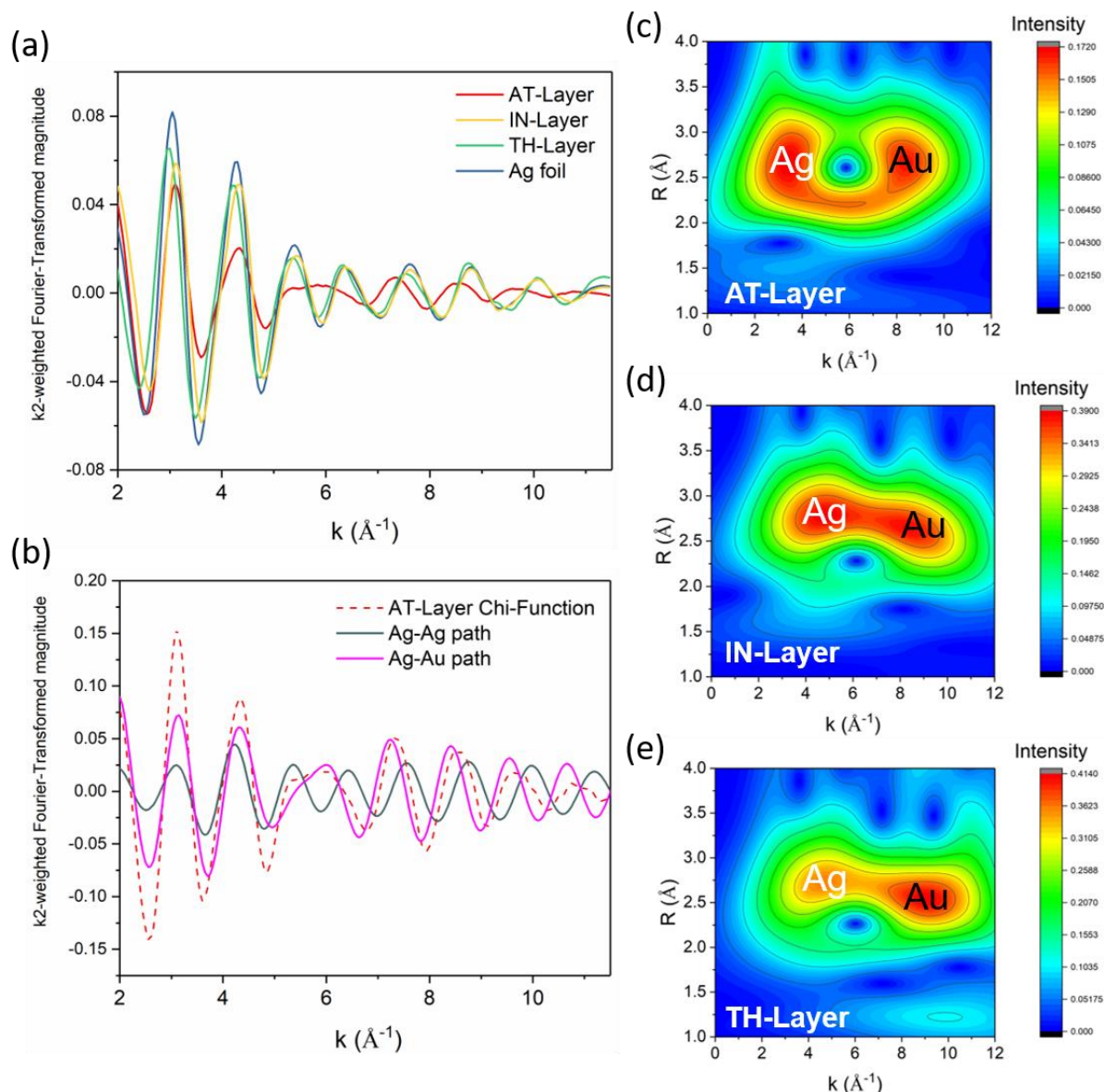


Figure 4. X-ray Absorption Spectroscopies for as-prepared core-shell samples. a) Fourier-Transformed (FT) k -space spectra (k^2 weighted) of the as-prepared core-shell NPs (AT-layer, IN-layer, TH-layer, and the reference Ag foil). b) FT k -space compositional spectra (k^2 weighted) of AT-layer with fitted Ag-Ag and Ag-Au scattering path contribution. c-e) Wavelet restoration for AT-layer, IN-layer, and TH-layer Au-Ag core-shell NPs respectively. Parameters used: R -range: 1-4, Morlet function, Kappa Morlet: 8, Sigma Morlet: 1.

Table 2. Least square fitting of the Ag K edge EXAFS spectra for the core-shell samples.

Ag K edge	Scattering Path	Bond length [Å]	Coordination number	Debye-Waller factor
AT-layer	Ag-Ag	2.88 (2)	2.1 (3)	0.005
	Ag-Au	2.89 (2)	5.7 (4)	0.005
IN-layer	Ag-Ag	2.86 (1)	11.1 (5)	0.010
	Ag-Au	2.89 (3)	1.8 (7)	0.010
TH-layer	Ag-Ag	2.87 (1)	11.4 (4)	0.009
	Ag-Au	2.90 (3)	1.1 (4)	0.003

Table 3. Least square fitting of the Au L₃ edge EXAFS spectra for the core-shell samples.

Au L ₃ edge	Scattering Path	Bond length [Å]	Coordination number	Debye-Waller factor
AT-layer	Au-Au	2.87 (1)	10.0 (4)	0.008
	Au-Ag	2.92 (1)	1.2 (5)	0.014
IN-layer	Au-Au	2.87 (1)	10.6 (4)	0.008
	Au-Ag	2.89 (4)	0.9 (4)	0.011
TH-layer	Au-Au	2.86 (1)	10.7 (7)	0.008
	Au-Ag	2.87 (1)	0.5 (6)	0.009

Apparently, from our results, both shell composition and thickness can critically affect EC-LSPR in capturing visible light energy at negative bias potential for HER.^[50] Discrete dipole approximation (DDA) was therefore briefly employed to model the induced electric fields of different shell thicknesses at 530 nm. This simulated model is based on Au-Ag core-shell nanoparticles with a 26.6 nm diameter of Au core with different shell thicknesses. From **Figure 5**, it can be observed that the maximum electric field strength (E^2) induced by LSPR occurs indeed takes place at the top atomic surface of NP on Au core. The DDA simulations show that the highest maximum E-field enhancements were detected for AT-layer Au-Ag nanoparticles. This agrees with the observation that this system enabled higher current enhancements, as higher LSPR-generated electric fields can enhance absorption and thus the generation of non-thermal hot electrons in these regions.^[57]

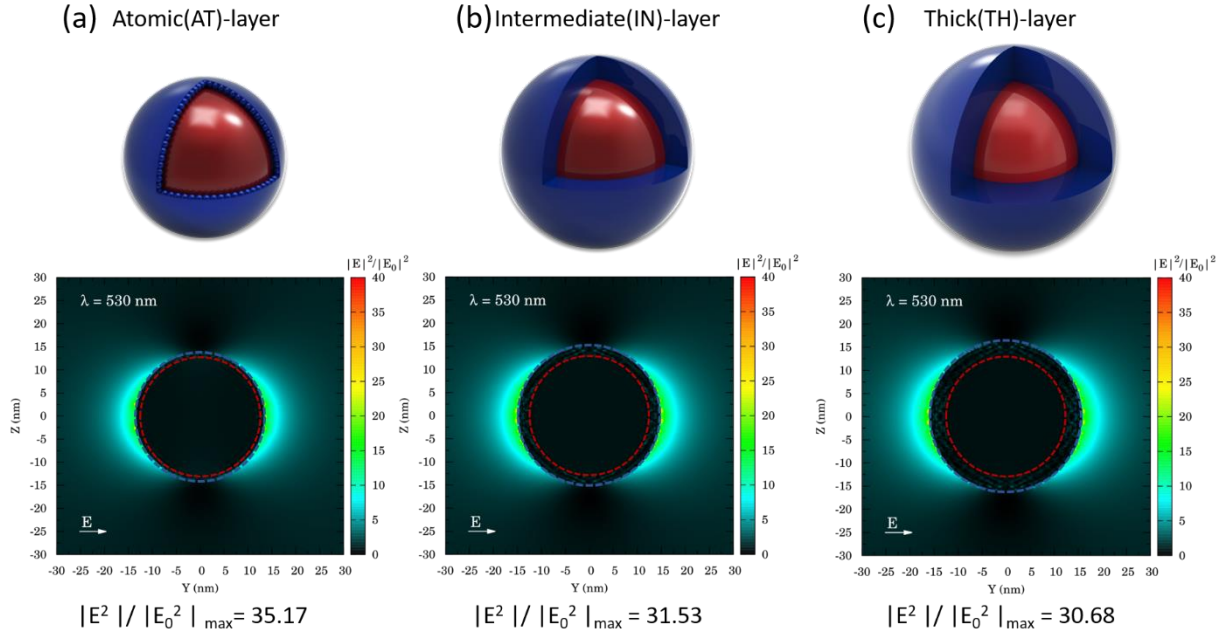


Figure 5. Induced electric field enhancement $|E^2|/|E_0^2|$ simulated by discrete dipole approximation (DDA) for Au-Ag core-shell NPs with overall 26.6 nm diameter of Au core and a) 1 nm Ag-shell (AT-layer), b) 3 nm Ag shell (IN-layer) and c) 5 nm Ag shell (TH-layer) at a wavelength of 530 nm.

To model how the shell composition can affect the electric field enhancement, DDA calculations have been performed with a model possessing the same shell thickness. Table S6 shows the variation of the induced electric field enhancement as a function of wavelength with different Au/Ag shell compositions of about 1 nm on 26 nm Au core. As the Ag concentration in the thin atomic shell increases, the field strength progressively resonates at lower wavelength, which agrees with the observed shifts of LSPR peak by UV-Vis studies shown in Figure 2a. Under UV-cut Tungsten light illumination as that of light-on experiments described in Table 1, electric field strength dramatically enhances when Ag is present in the shell, depicting the importance of Ag component in energy transfer at mixed Ag-Au surfaces. Hence, this result opens up further avenue to fine-tune the light absorption in EC-LSPR process by varying the shell composition.

3. Conclusion

To summarize, our study has clearly demonstrated the use of a novel EC-LSPR system for unprecedented performance in hydrogen evolution reaction under sunlight via a tailor-made core-shell material. A state-of-the-art atomic layer core-shell nanoparticle with precision-engineered Au/Ag composition on Au core has been successfully synthesized and characterized by STEM and APT, which enables the HEs generation excited by LSPR as evidenced by line-scanning STEM-EELS analysis. As a stable cathode catalyst, the AT-layer core-shell NPs exhibit impressive HER rate of $1870 \mu\text{mol g}^{-1}\text{h}^{-1}$ at room temperature under visible light, which is 112.5% increase when compared to light-off conditions, outperforming commercial Pt catalyst at 62.1% and most of those reported with semiconductor. The DDA simulation and X-ray absorption spectroscopy subsequently demonstrated the HEs induced by LSPR electric field is dependent on the shell chemical composition. Looking forward, metallic nanoparticles with variable chemical composition with or without dielectric support in the new EC-LSPR process may be used as a promising alternative to semiconductor for HER reaction due to their higher electron density, energy confinement and conductivity with no impedance.

4. Experimental Section

Materials: Trisodium citrate dehydrate ($\geq 99\%$, Sigma-Aldrich), gold(III) chloride trihydrate ($\geq 99.99\%$, Sigma-Aldrich), potassium hydroxide pellets (reagent grade, Fisher scientific), L-ascorbic acid ($\geq 99\%$, Sigma-Aldrich), silver nitrate ($\geq 99.9999\%$, Sigma-Aldrich), ethylene glycol (anhydrous, $\geq 99.8\%$, Sigma-Aldrich), polyvinylpyrrolidone (PVP, average Mw~55,000, Sigma-Aldrich), silver trifluoroacetate ($\geq 99.99\%$, Sigma Aldrich), sodium sulfate ($\geq 99\%$, Sigma-Aldrich), Vulcan carbon (Vulcan XC 72R, FuelCellStore), platinum on graphitized carbon (20 wt.% loading, Sigma Aldrich), 2-Propanol ($\geq 99.5\%$, Sigma Aldrich), Nafion perfluorinated resin solution (5wt.% in mixture of lower aliphatic alcohols and water, Sigma Aldrich), ethanol ($\geq 99.8\%$, Sigma Aldrich), Nitrogen gas (99.99%, BOC).

Synthesis of Catalysts: Au NPs were synthesized via the Citrate stabilized method. [38,58] 5 mg/mL sodium citrate was added into 95 mL deionized water then put in the oil bath at a temperature of 100 °C. Once the solution starts to boil, 2 mL of 25 mM $\text{HAuCl}_4 \cdot 3\text{H}_2\text{O}$ Au precursor was added into the reaction mixture and kept the temperature at 100 °C. The solution was boiled for 8 min and then cooled to room temperature.

The synthesis of Au-Ag core-shell NPs is based on the gradual reduction of Ag^+ ion on the as-prepared citrate-stabilized Au NPs through adding the AgNO_3 (Ag precursor) stepwise. For the first cycle, 150 μL of 0.1 M potassium hydroxide, 120 μL of 0.1 M ascorbic acid and 30 μL of 0.1 M silver nitrate were added into 10 mL of the as-prepared Au NPs at room temperature respectively, then reaction was stirred constantly for 30 min, namely Intermediate (IN)-layer Au-Ag core-shell sample. Repeat the cycles for three times with reaction time of 30 min for each cycle, the Thick (TH)-layer Au-Ag core-shell sample was obtained.

For the Atomic (AT)-layer of the Au-Ag core-shell NPs, 10 mL of the as-prepared Au NPs was added into a round bottom flask which was then placed in a sonication bath under ambient conditions. 150 μL of 0.1 M potassium hydroxide and 120 μL of 0.1M ascorbic acid were added into the flask followed by sonication (120 s). 30 μL of 0.01 M silver nitrate was then added into the flask and sonicated for another 120 s to obtain a well sonochemical dispersion of Ag. After that the mixture was stirred constantly for 30 min at room temperature.

Materials Characterization: Atomic-resolution EDS mapping was performed with an aberration-corrected scanning transmission electron microscope (S/TEM, Thermo Fisher Titan Themis Z 300) operated at 300 kV with a convergence semi-angle of 23.6 mrad. The high-angle annular dark-field scanning transmission electron microscopy (HAADF-STEM) imaging was carried out using a cold FEG aberration-corrected JEOL ARM200F. The microscope was operated at 200 kV in HAADF-STEM mode with HAADF detector collection semiangles from 73 to 271 mrad. Low-loss EELS were acquired by capturing many short acquisition spectra

(< 10 ms each) and then summing the spectra for a desired step size. The APT experiments were conducted in a CAMECA LEAP 5000 XR instrument at a specimen temperature of 50 K, a detection rate of 0.5, a pulsing rate of 125 kHz, and a laser pulse energy of 30 pJ. Data reconstruction and analysis were performed using the commercial IVAS 3.8.2™ software. The EXAFS spectra were measured in the fluorescence mode using a Lytle fluorescence detector for all metal samples. The demeter software package (ATHENA & ARTEMIS) was used to analyze the EXAFS data to obtain the local structural parameters.

Direct plasmonic electrochemical measurements: All the electrochemical measurements were determined using a potentialstat (AUTOLAB PGSTAT320N). A standard three-electrode photoelectrochemical cell was used in the experiment with core-shell NPs spray-casting onto the FTO glass as the working electrode, Ag/AgCl (sat.KCl) as the reference electrode, and a Pt electrode as the counter electrode. A solution of 0.5 M Na₂SO₄ (pH 6.5) was used as electrolyte without addition of any sacrificial reagents, which was purged continuously in flowing N₂. The temperature of the solution for the reaction was controlled by a flow of circling water connected to thermo-control devices to keep a constant reaction temperature of 298K. All the experiments were carried out at room temperature and inside a dark room to exclude the influence of background light. A UV-cut Tungsten light ($\lambda > 420$ nm) was used as a light source for the direct plasmonic electrochemical measurement and set up at a fixed distance of 5 cm from the catalyst-coated FTO working electrode. The amounts of hydrogen evolved were measured by gas chromatography (GC) equipped with thermoconductivity detectors (TCD) with N₂ as carrier gas.

Supporting Information

Supporting Information is available from the Wiley Online Library or from the author.

Acknowledgements

The authors wish to thank the National Synchrotron Radiation Research Center, Taiwan for SXRD beamline. The STEM-EELS facilities were provided by the David Cockayne Centre for Electron Microscopy of University of Oxford. The Super EDX analyses were provided by Materials Characterization Facility, Texas A&M University, USA. J.M. thanks Dr. Qianqi Ivana Lin for her suggestions in HER and LSPR experiments. W.X. and T.L. thank Deutsche Forschungsgemeinschaft (DFG) for financial support (project number 407513992) and Zentrum für Grenzflächendominierte Höchstleistungswerkstoffe (ZGH) at Ruhr University Bochum for the access to infrastructure (FEI Helios G4 CX FIB/SEM and Cameca LEAP 5000 XR). E.B. thanks FAPESP for the fellowships 2015/11452-5 and 2018/00393-6.

Declaration of Competing Interest

The authors declare no conflict of interest.

Received: ((will be filled in by the editorial staff))

Revised: ((will be filled in by the editorial staff))

Published online: ((will be filled in by the editorial staff))

References

- [1] Y. Ma, X. Wang, Y. Jia, X. Chen, H. Han, C. Li, *Chem. Rev.* **2014**, *114*, 9987.
- [2] Z. Pu, J. Zhao, I. S. Amiinu, W. Li, M. Wang, D. He, S. Mu, *Energy Environ. Sci.* **2019**, *12*, 952.
- [3] M. Cabán-Acevedo, M. L. Stone, J. R. Schmidt, J. G. Thomas, Q. Ding, H. C. Chang, M. L. Tsai, H. He, S. Jin, *Nat. Mater.* **2015**, *14*, 1245.
- [4] I. Dincer, C. Zamfirescu, *Sustainable Hydrogen Production*, 1st ed., Vol. 305, Elsevier, **2016**.
- [5] J. N. Tiwari, S. Sultan, C. W. Myung, T. Yoon, N. Li, M. Ha, A. M. Harzandi, H. J. Park, D. Y. Kim, S. S. Chandrasekaran, W. G. Lee, V. Vij, H. Kang, T. J. Shin, H. S. Shin, G. Lee, Z. Lee, K. S. Kim, *Nat. Energy* **2018**, *3*, 773.
- [6] K. H. A Fujishima, *Nature* **1972**, *238*, 38.

- [7] J. Ran, J. Zhang, J. Yu, M. Jaroniec, S. Qiao, *Chem. Soc. Rev.* **2014**, 43, 7787.
- [8] X. Li, J. Yu, J. Low, Y. Fang, J. Xiao, X. Chen, *J. Mater. Chem. A* **2015**, 3, 2485.
- [9] S. Chen, D. Huang, P. Xu, W. Xue, L. Lei, M. Cheng, R. Wang, X. Liu, R. Deng, *J. Mater. Chem. A* **2020**, 8, 2286.
- [10] M. R. Shaner, H. A. Atwater, N. S. Lewis, E. W. McFarland, *Energy Environ. Sci.* **2016**, 9, 2354.
- [11] Q. Wang, T. Hisatomi, Q. Jia, H. Tokudome, M. Zhong, C. Wang, Z. Pan, T. Takata, M. Nakabayashi, N. Shibata, Y. Li, I. D. Sharp, A. Kudo, T. Yamada, K. Domen, *Nat. Mater.* **2016**, 15, 611.
- [12] Y. Qiu, W. Liu, W. Chen, G. Zhou, P. C. Hsu, R. Zhang, Z. Liang, S. Fan, Y. Zhang, Y. Cui, *Sci. Adv.* **2016**, 2, e1501764.
- [13] M. J. Kale, T. Avanesian, P. Christopher, *ACS Catal.* **2014**, 4, 116.
- [14] L. Chang, L. V. Besteiro, J. Sun, E. Y. Santiago, S. K. Gray, Z. Wang, A. O. Govorov, *ACS Energy Lett.* **2019**, 4, 2552.
- [15] G. Liu, Y. Liu, J. Zhao, A. Pan, B. Wang, T. Zhu, *ACS Appl. Energy Mater.* **2020**, 3, 6146.
- [16] X. Li, S. Guo, C. Kan, J. Zhu, T. Tong, S. Ke, W. C. H. Choy, B. Wei, *Nano Energy* **2016**, 30, 549.
- [17] S. Mukherjee, F. Libisch, N. Large, O. Neumann, L. V Brown, J. Cheng, B. Lassiter, E. A. Carter, P. Nordlander, N. J. Halas, J. B. Lassiter, E. A. Carter, P. Nordlander, N. J. Halas, *Nano Lett.* **2013**, 13, 240.
- [18] L. Pang, A. Barras, V. Mishyn, G. Sandu, S. Melinte, P. Subramanian, R. Boukherroub, S. Szunerits, *J. Mater. Chem. A* **2020**, 8, 13980.
- [19] Y. Shi, J. Wang, C. Wang, T. T. Zhai, W. J. Bao, J. J. Xu, X. H. Xia, H. Y. Chen, *J. Am. Chem. Soc.* **2015**, 137, 7365.
- [20] S. S. Wang, L. Jiao, Y. Qian, W. C. Hu, G. Y. Xu, C. Wang, H. L. Jiang, *Angew. Chemie*

- *Int. Ed.* **2019**, 58, 10713.

- [21] P. Sriram, D. S. Su, A. P. Periasamy, A. Manikandan, S. W. Wang, H. T. Chang, Y. L. Chueh, T. J. Yen, *Adv. Energy Mater.* **2018**, 8, 1.
- [22] Y. Zhang, J. Du, R. Luo, Z. Wang, Z. Wang, J. Han, P. Liu, T. Fujita, Q. Xue, M. Chen, *Nano Energy* **2019**, 58, 552.
- [23] L. M. Liz-Marzán, *Langmuir* **2006**, 22, 32.
- [24] F. Gao, Y. Zhang, F. Ren, Y. Shiraishi, Y. Du, *Adv. Funct. Mater.* **2020**, 30, 2000255.
- [25] H. Wu, N. H. Alshareef, T. Zhu, *InfoMat* **2019**, 1, 417.
- [26] D. M. Mott, D. T. N. Anh, P. Singh, C. Shankar, S. Maenosono, *Adv. Colloid Interface Sci.* **2012**, 185–186, 14.
- [27] T. A. Taton, C. A. Mirkin, R. L. Letsinger, *Science* **2000**, 289, 1757.
- [28] X. Lu, M. Rycenga, S. E. Skrabalak, B. Wiley, Y. Xia, *Annu. Rev. Phys. Chem.* **2009**, 60, 167.
- [29] Q. Wang, Y. Lei, Y. Wang, Y. Liu, C. Song, J. Zeng, Y. Song, X. Duan, D. Wang, Y. Li, *Energy Environ. Sci.* **2020**, 13, 1593.
- [30] Y. Lei, Y. Wang, Y. Liu, C. Song, Q. Li, D. Wang, Y. Li, *Angew. Chemie - Int. Ed.* **2020**, 59, 20794.
- [31] D. Zheng, X. Cao, X. Wang, *Angew. Chemie - Int. Ed.* **2016**, 55, 11512.
- [32] W. Che, W. Cheng, T. Yao, F. Tang, W. Liu, H. Su, Y. Huang, Q. Liu, J. Liu, F. Hu, Z. Pan, Z. Sun, S. Wei, *J. Am. Chem. Soc.* **2017**, 139, 3021.
- [33] W. Fang, J. Liu, D. Yang, Z. Wei, Z. Jiang, W. Shangguan, *ACS Sustain. Chem. Eng.* **2017**, 5, 6578.
- [34] H. He, J. Cao, M. Guo, H. Lin, J. Zhang, Y. Chen, S. Chen, *Appl. Catal. B Environ.* **2019**, 249, 246.
- [35] Y. Zhong, Y. Wu, B. Chang, Z. Ai, K. Zhang, Y. Shao, L. Zhang, X. Hao, *J. Mater. Chem. A* **2019**, 7, 14638.

- [36] W. Liu, L. Cao, W. Cheng, Y. Cao, X. Liu, W. Zhang, X. Mou, L. Jin, X. Zheng, W. Che, Q. Liu, T. Yao, *Angew. Chemie - Int. Ed.* **2017**, *56*, 9312.
- [37] E. Article, G. Zhang, Z. Lan, L. Lin, S. Lin, X. Wang, *Chem. Sci.* **2016**, *7*, 3062.
- [38] A. K. Samal, L. Polavarapu, S. Rodal-Cedeira, L. M. Liz-Marzán, J. Pérez-Juste, I. Pastoriza-Santos, *Langmuir* **2013**, *29*, 15076.
- [39] M. B. Cortie, A. M. McDonagh, *Chem. Rev.* **2011**, *111*, 3713.
- [40] I. F. Teixeira, E. C. M. Barbosa, S. C. E. Tsang, P. H. C. Camargo, *Chem. Soc. Rev.* **2018**, *47*, 7783.
- [41] A. L. Koh, K. Bao, I. Khan, W. E. Smith, G. Kothleitner, P. Nordlander, S. A. Maier, D. W. McComb, *ACS Nano* **2009**, *3*, 3015.
- [42] R. Arenal, L. Henrard, L. Roiban, O. Ersen, J. Burgin, M. Treguer-Delapierre, *J. Phys. Chem. C* **2014**, *118*, 25643.
- [43] B. Schaffer, U. Hohenester, A. Trügler, F. Hofer, *Phys. Rev. B - Condens. Matter Mater. Phys.* **2009**, *79*, 1.
- [44] M. E. Sykes, J. W. Stewart, G. M. Akselrod, X. T. Kong, Z. Wang, D. J. Gosztola, A. B. F. Martinson, D. Rosenmann, M. H. Mikkelsen, A. O. Govorov, G. P. Wiederrecht, *Nat. Commun.* **2017**, *8*, 986.
- [45] X. T. Kong, Z. Wang, A. O. Govorov, *Adv. Opt. Mater.* **2017**, *5*, 1.
- [46] Y. Wu, G. Li, J. P. Camden, *Chem. Rev.* **2018**, *118*, 2994.
- [47] N. Mirsaleh-kohan, V. Iberi, P. D. Simmons, N. W. Bigelow, A. Vaschillo, M. M. Rowland, M. D. Best, S. J. Pennycook, D. J. Masiello, B. S. Guiton, J. P. Camden, *J. Phys. Chem. C* **2012**, *3*, 2303.
- [48] A. Pais, *Rev. Mod. Phys.* **1979**, *51*, 863.
- [49] A. Marzo, F. Beiza, P. Ferrada, J. Alonso, R. Roman, **2017**, 75830, 1.
- [50] N. Holmberg, K. Laasonen, P. Peljo, *Phys. Chem. Chem. Phys.* **2016**, *18*, 2924.
- [51] Q. Wu, J. Cao, X. Wang, Y. Liu, Y. Zhao, H. Wang, Y. Liu, H. Huang, F. Liao, M. Shao,

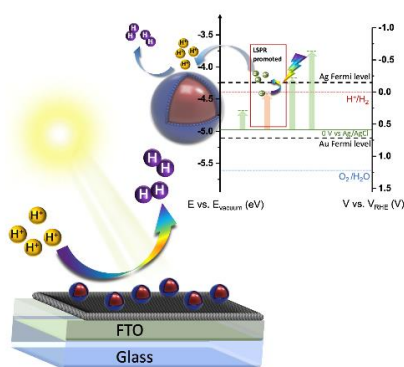
- Z. Kang, *Nat. Commun.* **2021**, *12*, 483.
- [52] J. Liu, Y. Liu, N. Liu, Y. Han, X. Zhang, H. Huang, Y. Lifshitz, S. T. Lee, J. Zhong, Z. Kang, *Science* **2015**, *347*, 970.
- [53] C. Li, T. Wang, Z. Luo, S. Liu, J. Gong, *Small* **2016**, *12*, 3415.
- [54] M. T. Sheldon, J. Van De Groep, A. M. Brown, A. Polman, H. A. Atwater, *Science* **2014**, *346*, 828.
- [55] S. Nootchanat, H. Ninsonti, A. Baba, S. Ekgasit, C. Thammacharoen, K. Shinbo, K. Kato, F. Kaneko, *Phys. Chem. Chem. Phys.* **2014**, *16*, 24484.
- [56] R. Compton, C. Banks, *Understanding Voltammetry*, 2nd ed., Imperial College Press, **2010**.
- [57] C. Clavero, *Nat. Photonics* **2014**, *8*, 95.
- [58] J. Turkevich, P. C. Stevenson, J. Hillier, *Discuss. Faraday Soc.* **1951**, *11*, 55.

An atomically-thin bimetallic-layered core-shell nanoparticle is developed via sonochemical dispersion. The Au-Ag shell gives rise to LSPR effect that transits hot electrons into low-lying excited state for efficient proton reduction with the aid of sunlight, which outperforms the commercial Pt catalyst by 62.1% in HER reaction, giving an excellent hydrogen production rate of $1870 \mu\text{mol g}^{-1}\text{h}^{-1}$ at room temperature.

Jiaying Mo, Eduardo C.M. Barbosa, Simson Wu, Yiyang Li, Yuancheng Sun, Weikai Xiang, Tong Li, Shengda Pu, Alex Robertson, Tai-sing Wu, Yun-liang Soo, Tiago V. Alves, Pedro H.C. Camargo, Winson Kuo, and Shik Chi Edman Tsang*

Atomic-Precision Tailoring of Au-Ag Core-shell Composite Nanoparticles for Direct Electrochemical-Plasmonic Hydrogen Evolution in Water Splitting

ToC figure



Supporting Information

Atomic-Precision Tailoring of Au-Ag Core-shell Composite Nanoparticles for Direct Electrochemical-Plasmonic Hydrogen Evolution in Water Splitting

Jiaying Mo, Eduardo C.M. Barbosa, Simson Wu, Yiyang Li, Yuancheng Sun, Weikai Xiang, Tong Li, Shengda Pu, Alex Robertson, Tai-sing Wu, Yun-liang Soo, Tiago V. Alves, Pedro H.C. Camargo, Winson Kuo, and Shik Chi Edman Tsang*

Supporting Information

Atomic-Precision Tailoring of Au-Ag Core-shell Composite Nanoparticles for Direct Electrochemical-Plasmonic Hydrogen Evolution in Water Splitting

Jiaying Mo¹, Eduardo CM Barbosa^{1,2}, Simson Wu¹, Yiyang Li¹, Yuancheng Sun¹, Weikai Xiang³, Tong Li³, Shengda Pu⁴, Alex Robertson⁴, Tai-sing Wu⁵, Yun-liang Soo⁵, Tiago. V. Alves⁶, Pedro HC Camargo^{2,7}, Winson Kuo⁸, Shik Chi Edman Tsang^{1*}

¹The Wolfson Catalysis Centre, Department of Chemistry, University of Oxford, Oxford, OX1 3QR, UK

*E-mail: edman.tsang@chem.ox.ac.uk

²Departamento de Química Fundamental, Instituto de Química, Universidade de São Paulo, São Paulo, SP, Brazil

³Institute for Materials, Ruhr Universität Bochum, Universitätsstr. 150, 44801 Bochum, Germany

⁴Department of Materials, University of Oxford, Oxford OX1 3PH, UK

⁵National Synchrotron Radiation Research Center, Hsinchu, Taiwan and Department of Physics, National Tsing Hua University, Hsinchu, Taiwan

⁶Departamento de Físico-Química, Instituto de Química, Universidade Federal da Bahia Rua Barão de Jeremoabo, 147, 40170-115, Salvador, BA, Brazil

⁷Department of Chemistry, University of Helsinki, A.I. Virtasen aukio 1, Helsinki, Finland

⁸Materials Characterization Facility, Texas A&M University, 3471 TAMU, College Station TX 77843, USA

1. Materials.

The reagents used are as followed: trisodium citrate dehydrate ($\geq 99\%$, Sigma-Aldrich), gold(III) chloride trihydrate ($\geq 99.99\%$, Sigma-Aldrich), potassium hydroxide pellets (reagent grade, Fisher scientific), L-ascorbic acid ($\geq 99\%$, Sigma-Aldrich), silver nitrate ($\geq 99.9999\%$, Sigma-Aldrich), ethylene glycol (anhydrous, $\geq 99.8\%$, Sigma-Aldrich), polyvinylpyrrolidone (PVP, average Mw~55,000, Sigma-Aldrich), silver trifluoroacetate ($\geq 99.99\%$, Sigma Aldrich), sodium sulfate ($\geq 99\%$, Sigma-Aldrich), Vulcan carbon (Vulcan XC 72R, FuelCellStore), platinum on graphitized carbon (20 wt.% loading, Sigma Aldrich), 2-Propanol ($\geq 99.5\%$, Sigma Aldrich), Nafion perfluorinated resin solution (5wt.% in mixture of lower aliphatic alcohols and water, Sigma Aldrich), ethanol ($\geq 99.8\%$, Sigma Aldrich), Nitrogen gas (99.99%, BOC).

2. Preparation of Au nanoparticles (NPs).

Citrate stabilized Au NPs were synthesized by the Turkevich method [1,2]. 5 mg/mL sodium citrate was added into 95 mL deionized water then put in the oil bath at a temperature of 100 °C. Once the solution starts to boil, 2 mL of 25 mM HAuCl₄·3H₂O Au precursor was added

into the reaction mixture and kept the temperature at 100 °C. The solution was boiled for 8 min and then cooled to room temperature.

3. Preparation of Ag nanoparticles (NPs).

The Ag nanoparticles were synthesized with the polyol process following the methods of Xia et al [3]. Ethylene glycol (EG, 5 mL) was added into a 25 mL round bottom flask and heated under magnetic stirring in an oil bath pre-set to 150°C. Poly(vinylpyrrolidone) (PVP, 1.25 mL, 20 mg/mL in EG) was injected into the reaction solution after 150°C was reached. After two minutes, CF₃COOAg (0.4 mL, 282 mM in EG) was added into reaction solution. 2 minutes later, the reaction solution was quenched by placing the flask in an ice-water bath. The sample was collected by centrifugation and then washed with acetone once, and with DI water four times.

4. Preparation of Au-Ag core-shell nanoparticles (NPs).

The synthesis of Au-Ag core-shell NPs is based on the gradual reduction of Ag⁺ ion on the as-prepared citrate-stabilized Au NPs through adding the AgNO₃ (Ag precursor) stepwise [2]. For the first cycle, 150 µL of 0.1 M potassium hydroxide, 120 µL of 0.1 M ascorbic acid and 30 µL of 0.1 M silver nitrate were added into 10 mL of the as-prepared Au NPs at room temperature respectively, then reaction was stirred constantly for 30 min, namely Intermediate (IN)-layer Au-Ag core-shell sample. Repeat the cycles for three times with reaction time of 30 min for each cycle, the Thick (TH)-layer Au-Ag core-shell sample was obtained.

For the Atomic (AT)-layer of the Au-Ag core-shell NPs, 10 mL of the as-prepared Au NPs was added into a round bottom flask which was then placed in a sonication bath under ambient conditions. Typically, 150 µL of 0.1 M potassium hydroxide and 120 µL of 0.1M ascorbic acid were added into the flask followed by sonication (120 s). 30 µL of 0.01 M silver nitrate was then added into the flask and sonicated for another 120 s to obtain a well sonochemical

dispersion of Ag. This is to ensure the reduction of Ag^+ onto the Au cores while inhibit the formation of free Ag nuclei. After that the mixture was stirred constantly for 30 min at room temperature.

The above prepared sample were supported on the Vulcan carbon via wet impregnation method as 20 wt% Au/C, 20 wt% Ag/C, 20 wt% AT-layer Au-Ag core-shell/C, 20 wt% IN-layer Au-Ag core-shell /C, 20 wt% TH-layer Au-Ag core-shell/C for electrochemistry reactions.

5. Titan STEM and Super X EDS Acquisition.

Atomic-resolution EDS mapping was performed with an aberration-corrected scanning transmission electron microscope (S/TEM, Thermo Fisher Titan Themis Z 300) operated at 300 kV with a convergence semi-angle of 23.6 mrad. The microscope was aligned before every experiment by using a gold standard sample ensuring 0.06 nm resolution under normal conditions. EDS analysis was carried out from its highly sensitive Super X detector which contains a high-speed, high-throughput, quad-silicon drift detector optimized for rapid x-ray collection (0.9 srad) and when combined with STEM enables EDS spectral mapping down to the atomic scale. The microscope was set to C2 aperture at 70 μm with beam current was set between 150~200 pA during the EDS data acquisition. The dwell time was set to 100 μs per pixel with a map size of 256×256 pixels; a complete process of EDS mapping took roughly 1 h to reach an appropriately high signal-to-noise ratio.

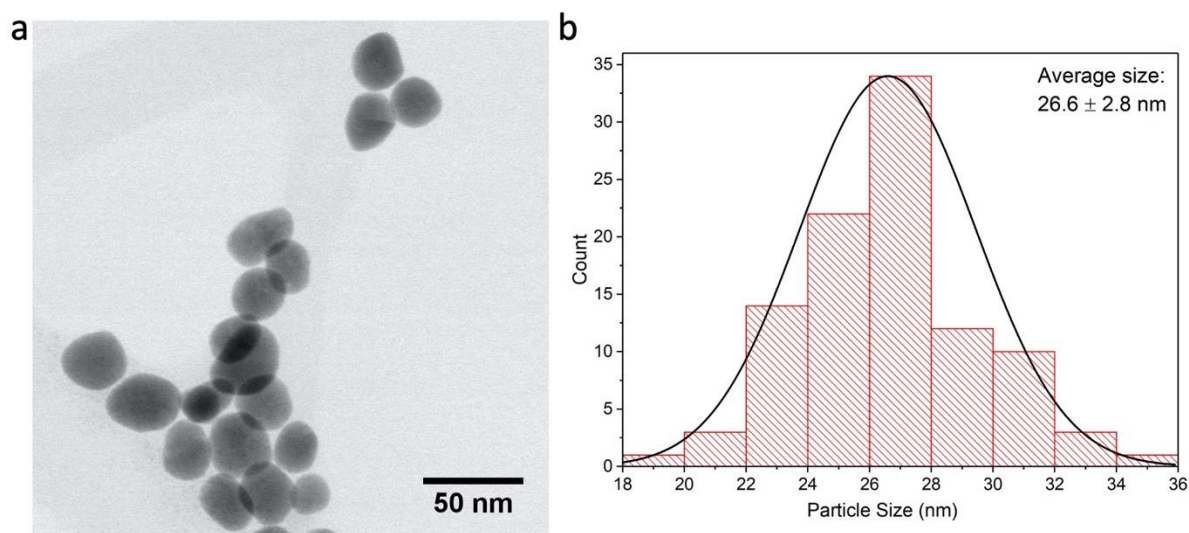


Figure S1. TEM image (a) of pure Au nanoparticles and corresponding histogram of size distribution (b).

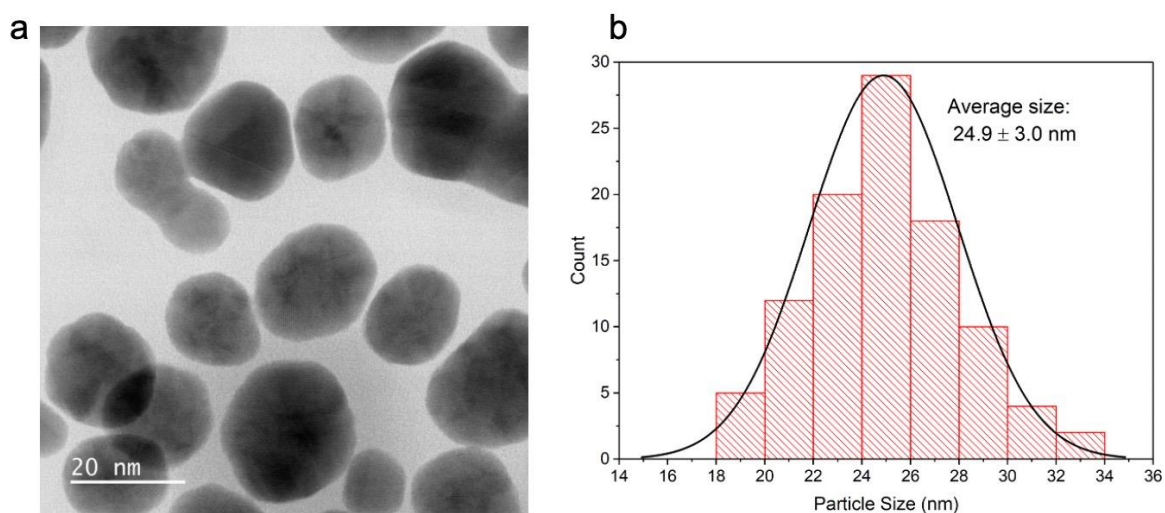


Figure S2. TEM image (a) of pure Ag nanoparticles and corresponding histogram of size distribution (b).

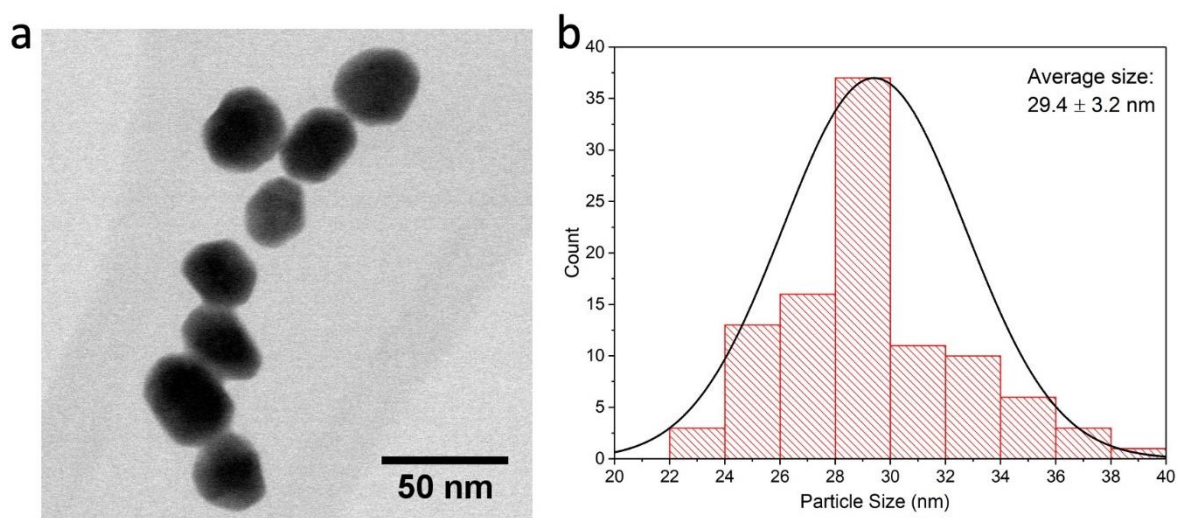


Figure S3. a) TEM image of AT-layer Au-Ag core-shell nanoparticles and corresponding histogram of size distribution (b) with a mean Ag shell thickness of 1.4 nm.

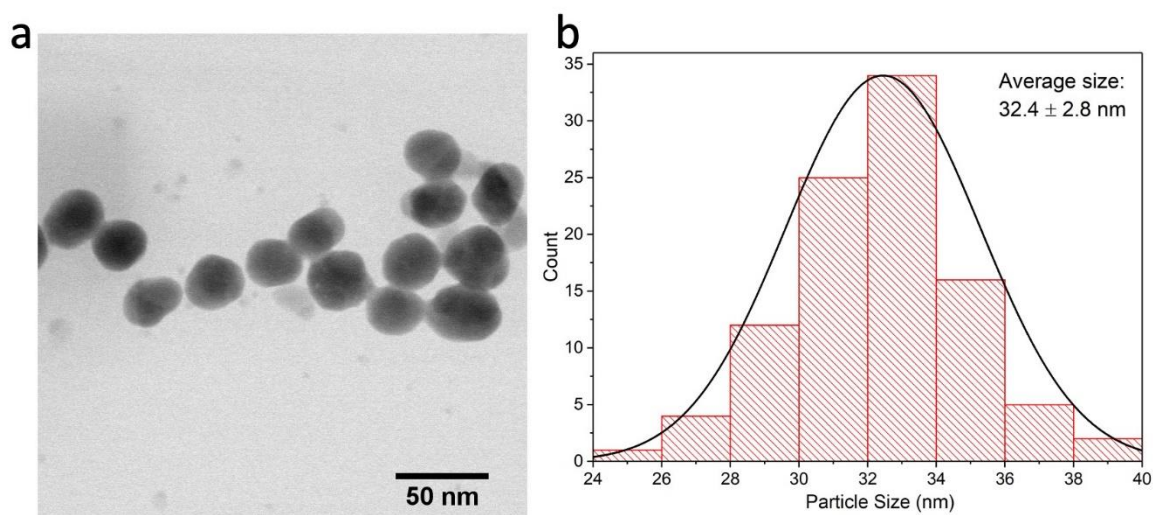


Figure S4. a) TEM image of IN-layer Au-Ag core-shell nanoparticles and corresponding histogram of size distribution (b) with a mean Ag shell thickness of 2.9 nm.

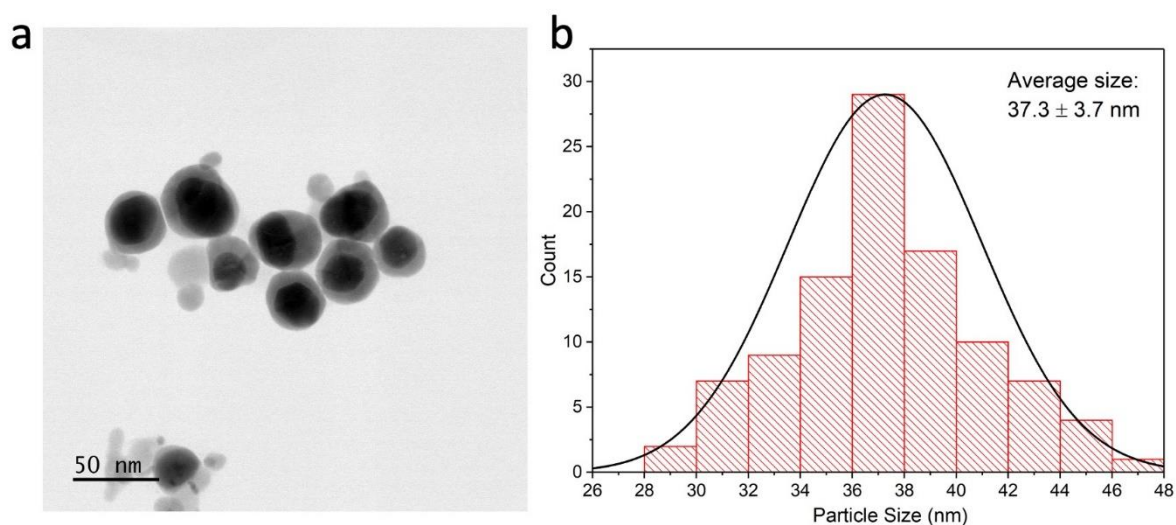


Figure S5. a) TEM image of TH-layer Au-Ag core-shell nanoparticles and corresponding histogram of size distribution (b) with a mean Ag shell thickness of 5.4 nm.

There was a small degree of size discrepancy in the analysis between EDX and APT profiling due to non-uniformity in core and size dimensions. As shown in typical Figure 1, the interfaces between core and shell materials are clearly shown to be non-uniform. There are thicker shell thicknesses in some regions than others.

6. Atom probe tomography (APT).

APT relies on generating high electric fields ($\sim 3\text{--}5 \text{ V } \text{\AA}^{-1}$) at the apex of a needle-shaped specimen. On top of this, an additional short (ns) voltage or laser pulse was applied to remove ions in a controlled manner into a high-resolution time-of-flight mass spectrometer equipped with a single-ion-sensitive detector. APT thus can provide 3D elemental mapping with single-atom sensitivity.

To prepare the APT specimens, nanoparticles were first distributed on a Ni-coated Si flat wafer and subsequently embedded by a 150-nm thick protective Ni layer in Leica EM ACE600 high vacuum sputter coater [4]. The needle-shaped APT specimens were then prepared by a standard lift-out procedure using a focused ion beam/scanning electron microscope (FIB/SEM) in FEI G4 CX. The APT experiments were conducted in a CAMECA LEAP 5000 XR instrument at a specimen temperature of 50 K, a detection rate of 0.5, a pulsing rate of 125 kHz, and a laser pulse energy of 30 pJ. Data reconstruction and analysis were performed using the commercial IVAS 3.8.2TM software.

7. High-resolution scanning transmission electron microscopy (STEM-EELS).

The high-angle annular dark-field scanning transmission electron microscopy (HAADF-STEM) imaging was carried out using a cold FEG aberration-corrected JEOL ARM200F. The microscope was operated at 200 kV in HAADF-STEM mode with HAADF detector collection semiangles from 73 to 271 mrad. Low-loss EELS were acquired by capturing many short acquisition spectra (< 10 ms each) and then summing the spectra for a desired step size. This avoided saturation of the zero-loss peak, and minimized the zero-loss peak FWHM, while still giving satisfactory signal-to-noise. Rather than using Digital Micrograph's inbuilt live spectral averaging feature, which did not sufficiently account for energy drift, we 'over-sampled' many spectra along a line scan (e.g. using a step size of 0.01 nm to effectively acquire 50 spectra per 0.5 nm) and aligned and summed offline using Digital Micrograph. A detailed discussion of this method is found [5]. EELS were acquired with a 20 meV dispersion at 200 keV and using a 2.5 mm entrance aperture.

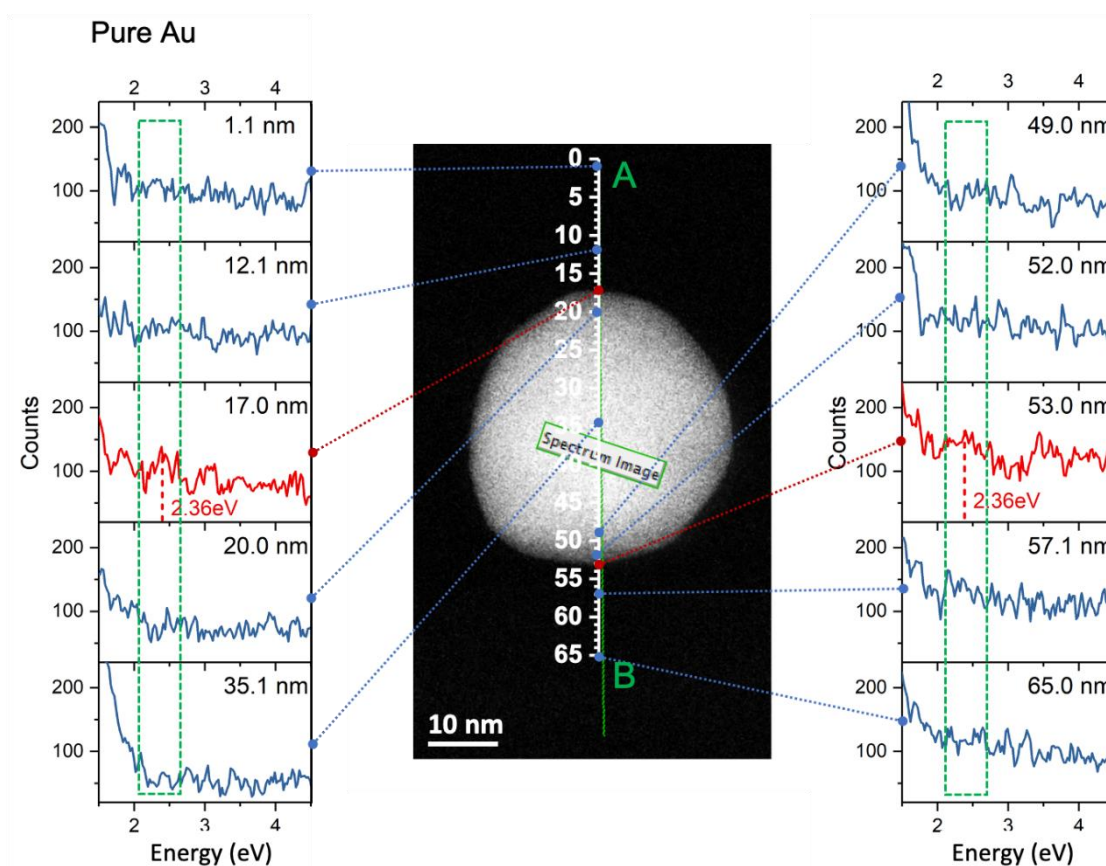


Figure S6. A series of 10 successive low-loss STEM-EEL spectra acquired of a single pure Au nanoparticle, in the spectrum-image mode, along an axis (A to B) of the nanosphere as illustrated in the inset. The position of the main resonance detected along the line scan are marked by green dotted lines.

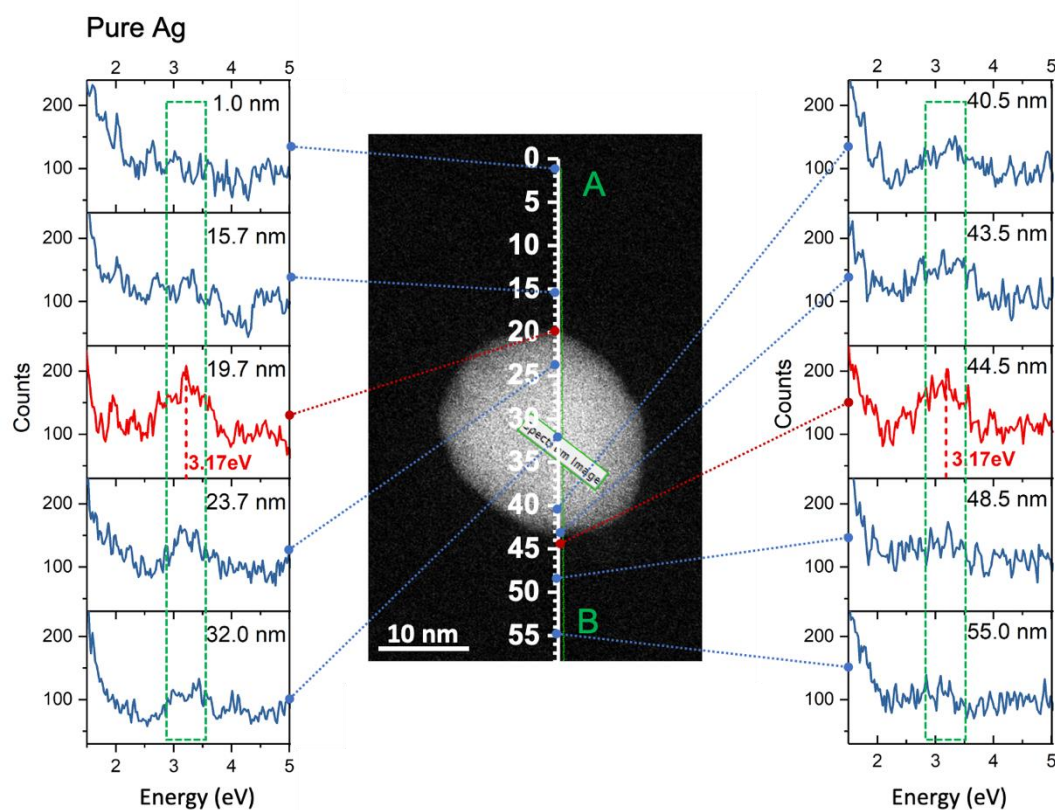


Figure S7. A series of 10 successive low-loss STEM–EEL spectra acquired of a single pure Ag nanoparticle, in the spectrum-image mode, along an axis (A to B) of the nanosphere as illustrated in the inset. The position of the main resonance detected along the line scan are marked by green dotted lines.

8. Direct Plasmonic Chronoamperometry.

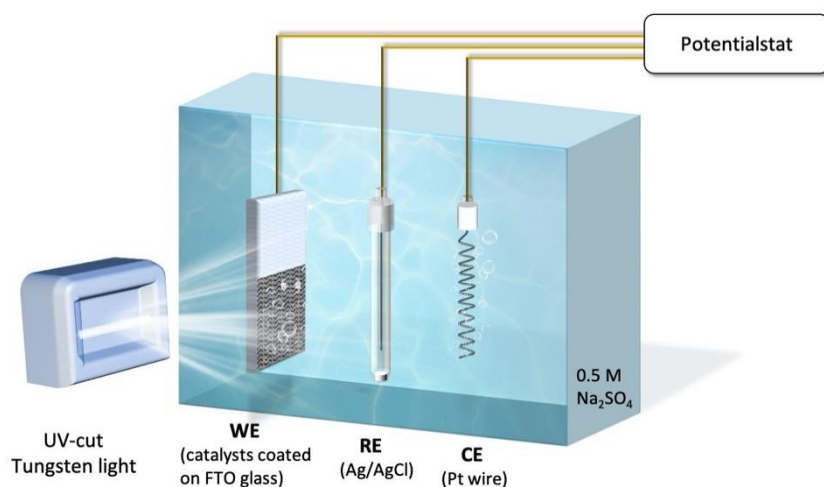


Figure S8. Schematic illustration of the three-electrode system with UV-cut Tungsten light as light source for the direct plasmonic chronoamperometry analysis.

All the electrochemical measurements were determined using a potentialstat/ galvanostat (AUTOLAB PGSTAT320N). A standard three-electrode photoelectrochemical cell was used in the experiment, where the core-shell nanoparticles spray-casting onto the FTO glass were used as the working electrode, Ag/AgCl (saturated KCl) as the reference electrode, and a Pt electrode as the counter electrode. A solution of 0.5 M Na_2SO_4 (pH 6.5) was used as electrolyte without any addition of sacrificial reagents, which was purged continuously in flowing N_2 to remove O_2 prior to the start of reaction. The temperature of the solution for the reaction was controlled by a flow of circling water connected to thermo-control devices to keep a constant reaction temperature of 298K. All the experiments were carried out at room temperature and inside a dark room to exclude the influence of background light. The working electrode were prepared as followed: First, fluoride tin oxide (FTO) glass was washed sequentially with acetone, ethanol and DI water in an ultrasonic bath for 30 min. Next, 10 mg of photocatalysts and 80 μL of 5 wt% Nafion solution were added into 2 mL ethanol and sonicated for 30 min to

obtain a catalyst ink. Then, 200 μL of the as-prepared catalyst ink was spray-casted directly onto the pre-cleaned FTO glass surface (1cm^2) and was air-dried (loaded about $0.2 \pm 0.08\text{ mg}\cdot\text{cm}^{-2}$ metal) before measurement. A UV-cut Tungsten light (Glamox Professional 2000, $\lambda > 420\text{ nm}$) with a power intensity of 110 mW cm^{-2} was used as a light source for the direct plasmonic electrochemical measurement and set up at a fixed distance of 5 cm from the catalyst-coated FTO working electrode. Additionally, an Oriel[®] solar simulator (1 sun, AM 1.5G, 100 mW cm^{-2}) was used to irradiate the working electrode at different wavelength ranges to further analyse the photocurrent/current density enhancement. The amounts of hydrogen evolved were measured by gas chromatography (GC) equipped with thermoconductivity detectors (TCD) with N_2 as carrier gas. The current density with/without light illumination on working electrode was recorded with chronoamperometry at a potential range of -0.3 V, -0.5 V, -0.8 V and -1.2 V respectively with a time interval of 200 s for stabilization.

Table S1. Photocatalytic hydrogen evolution (PHE) rates for AT-layer Au-Ag core-shell NPs under visible-light illumination at different applied potentials (vs Ag/AgCl) detected by GC-TCD.

Applied potential/ V	0	-0.5	-0.8	-1.2
PHE rate/ $\mu\text{mol h}^{-1} \text{g}^{-1}$	0	934 \pm 61	948 \pm 56	2432 \pm 201

At -0.5 V applied bias potential under visible light illumination, the overall hydrogen evolution rate of AT-layer Au-Ag core-shell NPs detected by GC-TCD is 1870 \pm 142 $\mu\text{mol h}^{-1} \text{g}^{-1}$.

In addition, we have also tried to calculate the photocatalytic hydrogen evolution (PHE) rates using the photocurrent (illumination current – dark current) as follows:

$$\text{HER rate} = \frac{\text{Charge (Q)}}{\text{Faraday constant} \times 2} = \frac{I_{ph} \times t}{2F} \text{ mol per time}$$

Where I_{ph} is the photocurrent, t is time and F is Faraday constant of 96485 C mol⁻¹.

For example, under an applied potential of -1.2 V, the AT-layer gives 143.3 μA of photocurrent under visible-light illumination with a working electrode area of 1 cm², such that the calculated hydrogen evolution rate is 2.67 $\mu\text{mol h}^{-1}$ (equivalent to 2673 $\mu\text{mol h}^{-1} \text{g}^{-1}$).

According to the above formula, the PHE rate is calculated from the photocurrent and summarized in Table S2.

Table S2. Photocatalytic hydrogen evolution (PHE) rate calculated from the above formula for AT-layer under visible-light illumination at different applied potential (vs Ag/AgCl).

Applied potential/ V	-0.5	-0.8	-1.2
PHE rate/ $\mu\text{mol h}^{-1} \text{g}^{-1}$	1026	1031	2673

The difference between the photocatalytic hydrogen evolution amount detected by GC analysis and the photocurrent calculations is found to be less than 10%. It thus strongly suggests that the photocurrent generated under visible light illumination at ambient temperature corresponds mainly to the LSPR-excited electrons for proton reductions.

Table S3. Photocatalytic hydrogen evolution rate ($\mu\text{mol h}^{-1}\text{g}^{-1}$) of different photocatalysts under UV/Visible light illumination at room temperature without any sacrificial reagent in the photocatalysis system.

Catalyst/-structure	Temperature	Light source	Sacrificial reagent	H ₂ Rate ($\mu\text{mol h}^{-1}\text{g}^{-1}$)	Ref.
LaMnO ₃	RT	simulated sunlight (AM 1.5G)	N/A	103	[6]
ZnTiO ₃	RT	254nm UV pen-ray lamp	N/A	156.7	[7]
CdS/Ni ₂ P/g-C ₃ N ₄	RT	Xe lamp ($\lambda > 420\text{nm}$)	N/A	15.56	[8]
CoP/CdS/WS ₂	RT	Xe lamp ($\lambda > 420\text{nm}$)	N/A	9.16	[9]
Co ₁ -phosphide/PCN	288K	visible light ($\lambda > 420\text{nm}$)	N/A	126.8	[10]
Ni@NiO _x -SrTiO ₃	RT	Solar simulator (AM 1.5)	N/A	18	[11]
Co ₃ O ₄ /HCNS/ Pt hybrids	RT	UV irradiation ($\lambda > 300\text{nm}$)	N/A	155	[12]
Bi _x Y _{1-x} VO ₄ solid solution	RT	Xe lamp ($\lambda > 300\text{nm}$)	N/A	1390	[13]
Pt/g-C ₃ N ₄	RT	Xe lamp UV ($\lambda > 300\text{nm}$)	N/A	61	[14]
Pt/g-C ₃ N ₄	RT	Xe lamp visible light ($\lambda > 420\text{nm}$)	N/A	6	[14]
(Cring)-C ₃ N ₄ P	RT	Xe lamp visible light ($\lambda > 420\text{nm}$)	N/A	150	[15]
(Cring)-C ₃ N ₄ P	RT	Xe lamp (solar AM 1.5)	N/A	371	[15]
CoP/g-C ₃ N ₄	RT	Xe lamp ($\lambda > 300\text{nm}$)	N/A	250	[16]
TiO ₂ /C ₃ N ₄ -Ni(OH) ₂ /WO ₃ (PtO _x)	298K	Xe lamp ($\lambda > 200\text{nm}$)	N/A	251	[17]
TiO ₂ /g-C ₃ N ₄ -WO ₃	298K	Xe lamp ($\lambda > 200\text{nm}$)	N/A	29.4	[17]
TiO ₂ /g-C ₃ N ₄ -Ni(OH) ₂ /WO ₃	298K	Xe lamp ($\lambda > 200\text{nm}$)	N/A	49	[17]
AT-layer Au-Ag/C at -0.5 V	298K	Tungsten light ($\lambda > 420\text{nm}$)	N/A	934	This work
AT-layer Au-Ag/C at -0.5 V overall electrolysis*	298K	Tungsten light ($\lambda > 420\text{nm}$)	N/A	1870	This work
AT-layer Au-Ag/C at -0.8 V	298K	Tungsten light ($\lambda > 420\text{nm}$)	N/A	948	This work
AT-layer Au-Ag/C at -1.2 V	298K	Tungsten light ($\lambda > 420\text{nm}$)	N/A	2432	This work

*Overall hydrogen evolution rate of the AT-layer Au-Ag core-shell NPs at -0.5 V_{Ag/AgCl} electrolysis under visible light illumination.

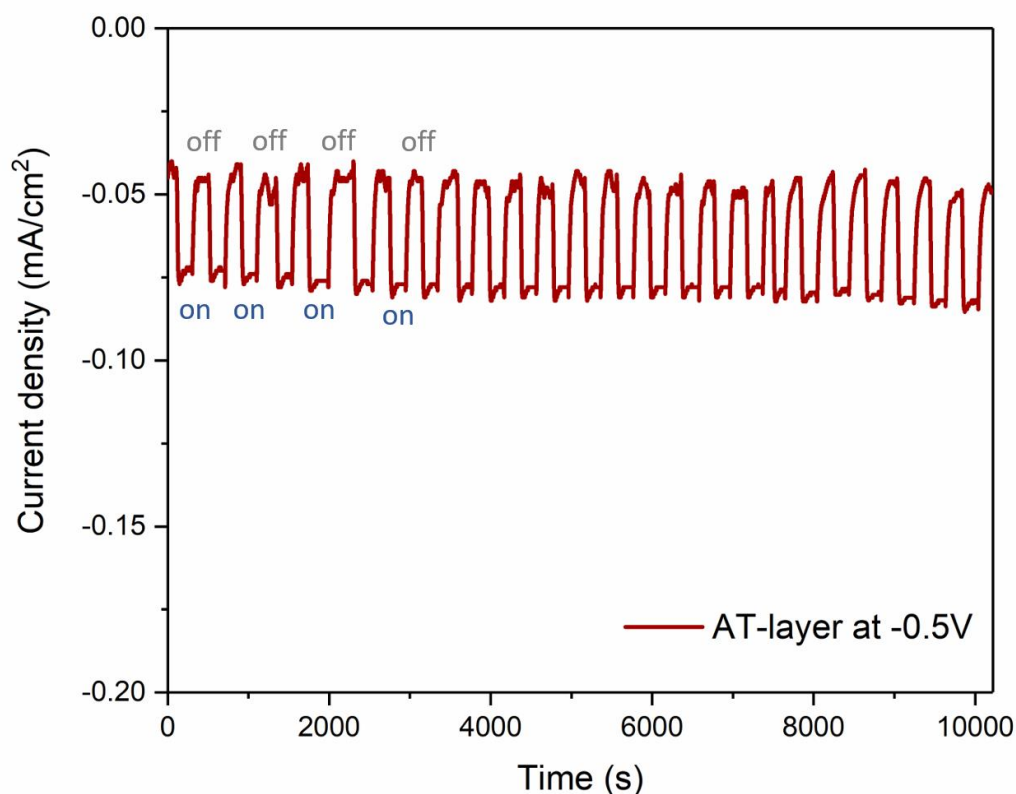


Figure S9. The cycling stability test of AT-layer Au-Ag core-shell NPs at -0.5 V versus Ag/AgCl under visible light ($\lambda > 420$ nm) illuminations with around 200-seconds on-off cycles.

In order to evaluate the cycling stability of the Au-Ag core-shell materials, a separate experiment was performed on the AT-layer Au-Ag core-shell NPs under identical experimental conditions (Figure S8) at an applied potential of -0.5 V vs Ag/AgCl for around 10000 s with interval of 200-seconds on-off cycles. As it shows in Figure S9, the transient photocurrent responses under visible light illumination are stable with negligible fluctuations, and the 200-seconds on-off cycles of photocurrents are again reproducible.

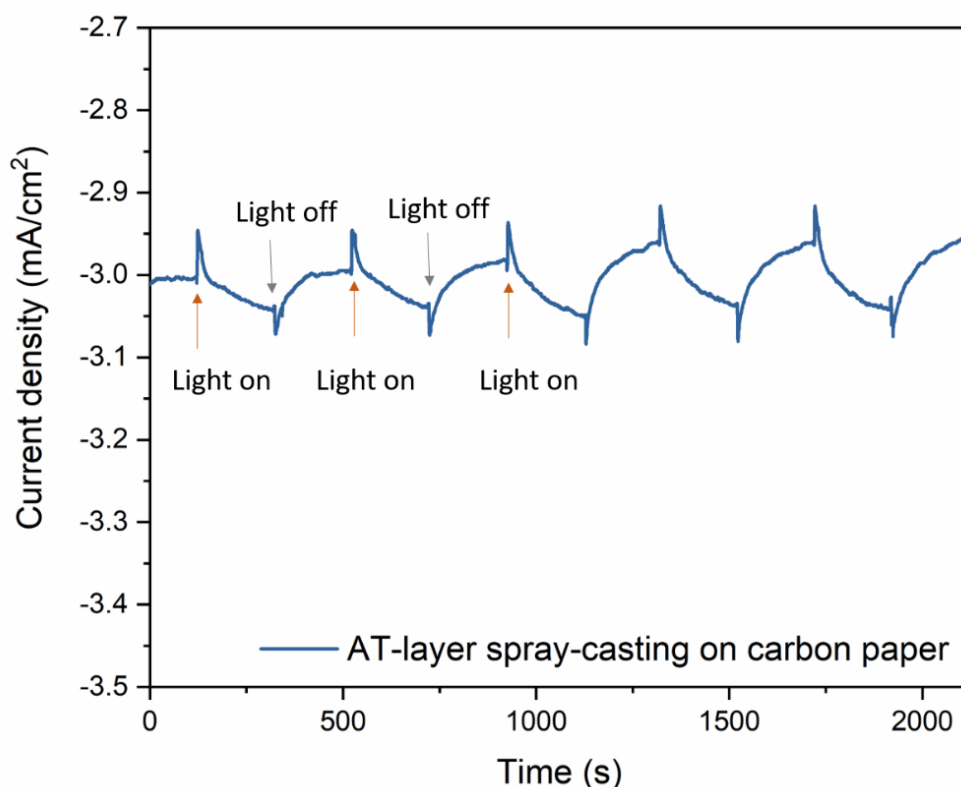


Figure S10. Current density of AT-layer Au-Ag core-shell NPs using carbon paper (instead of FTO glass) as working electrode under UV-cut Tungsten light ($\lambda > 420$ nm) illumination at -0.3 V applied bias potential.

In order to further assess the role of the FTO glass in the system, we have performed additional experiments using carbon paper (Sigracet 39BC) to replace the FTO glass as a working electrode under identical experimental conditions. The result (Figure S10) indeed displays similar phenomenon of the light on/off cycles in that the current density increases as visible light illuminated on the catalyst. As a result, this indicates that the FTO glass play little role in the electrochemical activity given its similar performance as the carbon paper. It is worthwhile to note that the extent of current increase in the case of carbon paper is different from that of FTO glass. This is because of the significant difference in conductivity between carbon paper and the FTO glass. Hence, the more conductive carbon paper results in a less extent of polarisation that leads to a smaller percentage change in current density enhancement.

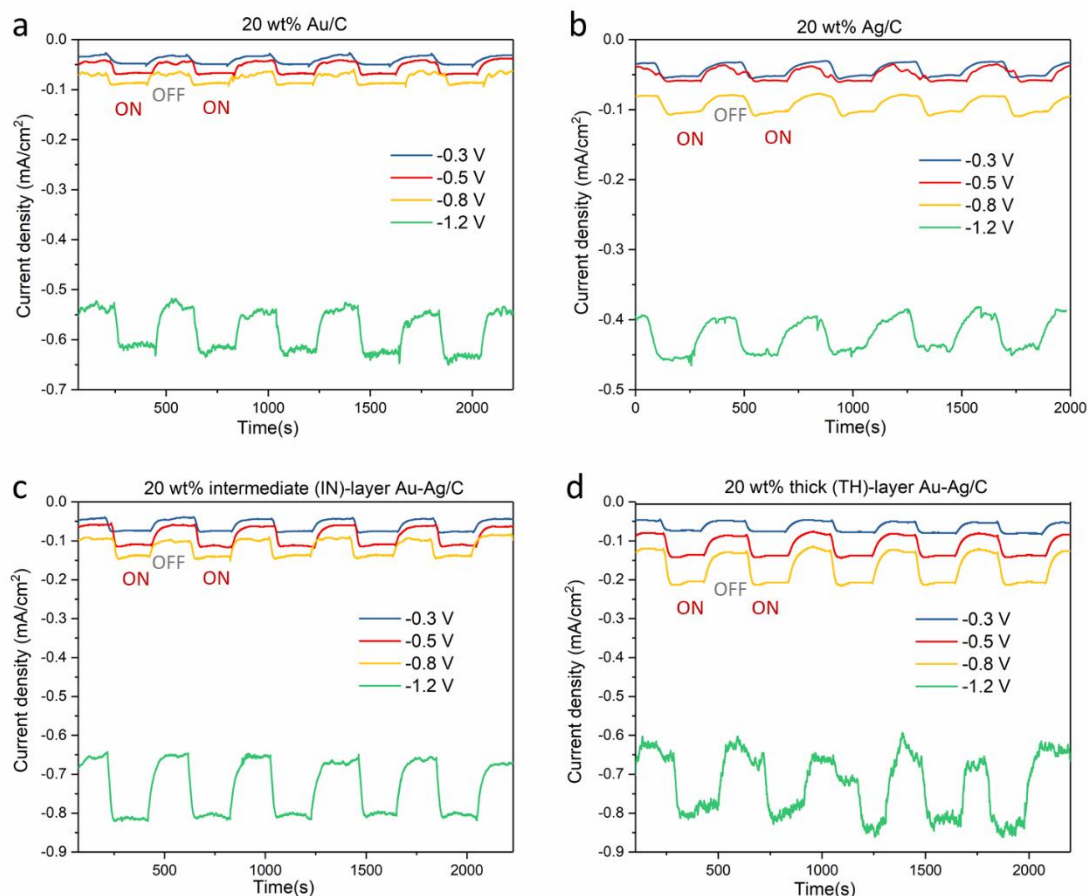


Figure S11. Current density as a function of reaction time of a) 20 wt% pure Au/C, b) 20 wt% pure Ag/C, c) 20 wt% IN-layer Au-Ag NPs/C and d) 20 wt% TH-layer Au-Ag NPs/C at -0.3 V, -0.5 V, -0.8 V and -1.2 V respectively under UV-cut Tungsten light.

In the direct EC-LSPR experiment, a negative potential (e.g., -0.3, -0.5, -0.8 and -1.2 V vs Ag/AgCl) was applied to the Au-Ag core-shell working electrode, giving a cathodic photocurrent under visible light illumination. This enhancement in cathodic photocurrent is caused by LSPR generated hot-electrons that have been transferred to the electron acceptors (H^+) in the system under visible light illuminations [18].

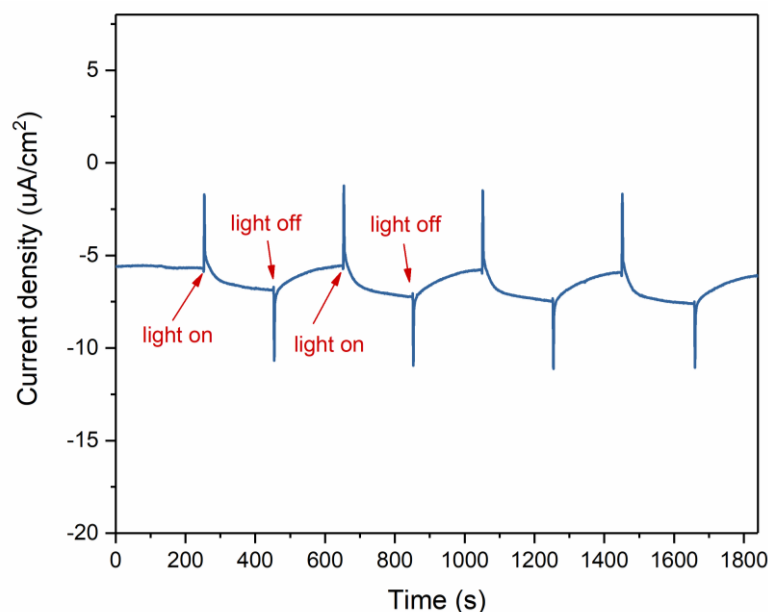


Figure S12. Current density of AT-layer Au-Ag core-shell NPs under UV-cut Tungsten light ($\lambda > 420$ nm) illumination at 0 V applied bias potential.

We further performed an experiment on the AT-layer Au-Ag core-shell NPs at 0 V applied bias potential under on/off illumination cycles to evaluate the maximum temperature effect, if any of the system. Under such conditions, no H_2 evolution (according to GC-TCD analysis) was detected at 0 V bias potential with or without light illumination. As shown in Figure S12, there is a very small thermal photocurrent (in $\sim 6 \mu\text{A}/\text{cm}^2$) recorded in dark conditions. Apart from the transient current disturbance, there is a net increase in current density reaching $1.68 \mu\text{A}/\text{cm}^2$ under visible light illumination. Thus, this magnitude of the photocurrent increase observed under 0 V may represent the highest thermal effect from light illumination due to the temperature rise caused by nonradiative thermal energy transfer of Ag/Au NPs [19]. Such magnitude of the thermal induced current density ($1.68 \mu\text{A}/\text{cm}^2$) observed in Figure S12 is negligible as it only contributes around 2 % of the measured photocurrent. It is also worthwhile to point out that the temperature of the reaction set-up was properly maintained at 298 K by a flowing water circulation connected to thermo-control devices. All throughout this study, we used the UV-cut light source to minimise such absorption.

Table S4. The EC-LSPR current density enhancement of AT-layer Au-Ag supported on Vulcan carbon at applied potential of 0 V, -0.3 V, -0.5 V, -0.8 V and -1.2 V, respectively under UV-cut Tungsten light compared with no light illumination.

Applied potentials	0 V	-0.3 V	-0.5 V	-0.8 V	-1.2 V
Current density enhancement	29.1%	82.1%	112.5%	73.8%	26.1%

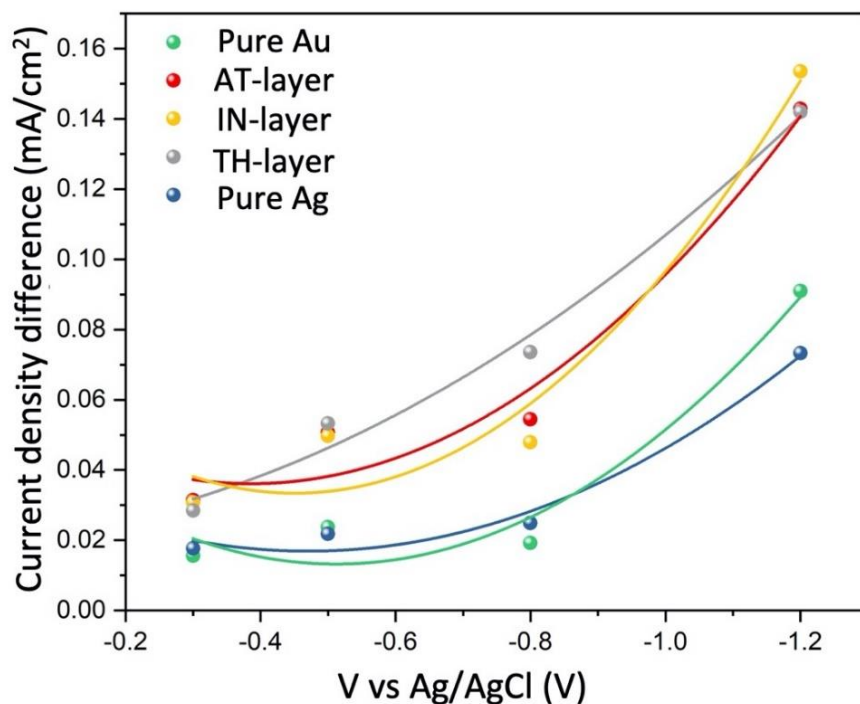


Figure S13. Current density difference (current density at light on minus current density at light off) as a function of applied negative bias potential of 20 wt% pure Au/C, 20 wt% pure Ag/C, 20 wt% AT-layer, IN-layer and TH-layer Au-Ag NPs /C at -0.3 V, -0.5 V, -0.8 V and -1.2 V respectively under UV-cut Tungsten light.

As seen from Figure S13, the higher degree of polarization at stronger bias potential clearly gives higher current density when light is on compared to light off for all samples. This suggests that the LSPR for non-thermal hot electrons for protons reduction can be proportionally promoted in negative bias potential, suggesting this charge separation process is fundamentally favoured. Notice that mixed Ag/Au atoms in core-shell samples outperform their pure Au and Ag NPs counterparts as the hot electrons generated depend on their chemical composition. However, TH-layer shows higher current values than expected presumably, additional pure Ag NPs from the poor core shell synthesis due to excessive addition of Ag precursors (refer to Figure S5a)) can enhance the light excitation by the increasing number of total number of NPs in this case.

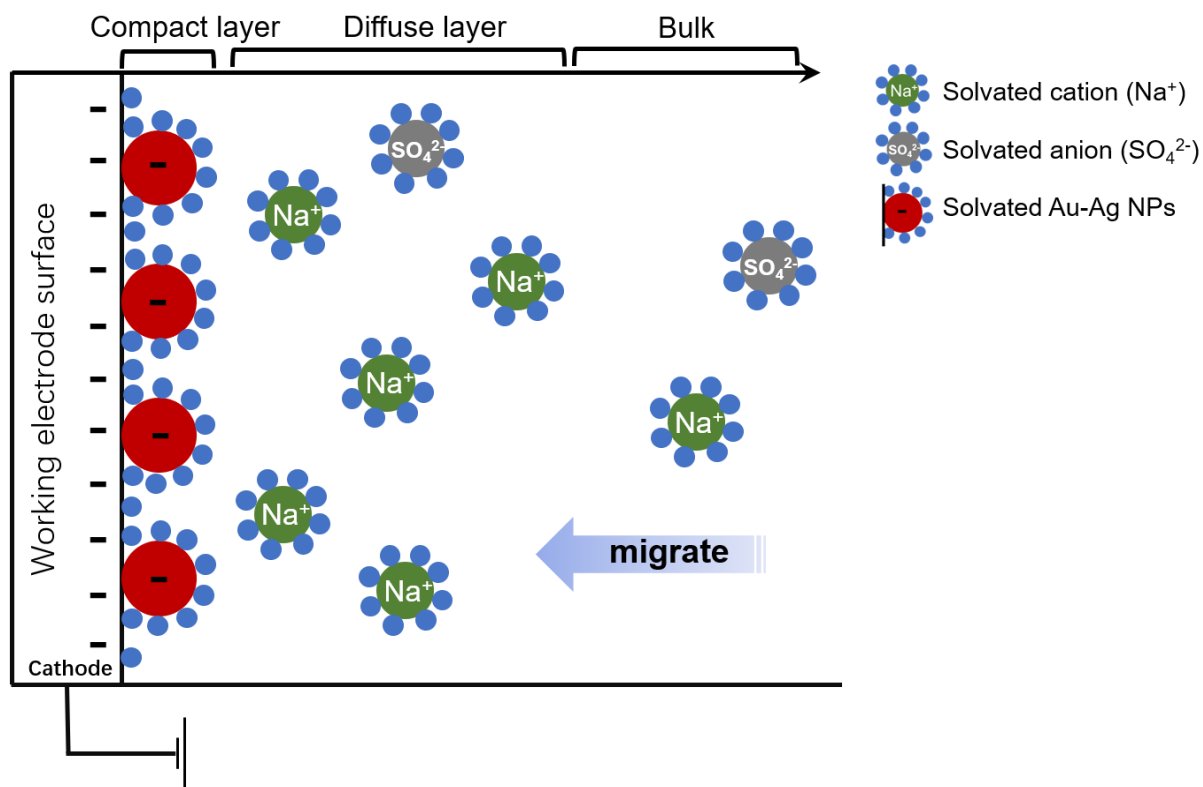


Figure S14. Schematic representations of electric double layer structures according to the Gouy–Chapman electrical double layer model.

Theoretically, the Gouy–Chapman model is a diffuse model of the electrical double layer, in which the electric potential decreases exponentially as the distance from the surface is increased assuming that the ions are point charges (as such finite ion size is ignored) [20]. As a result, it can be expected that the concentration of the counter-ions is higher near the surface than in the bulk solution. (Please refer to Figure S14 for a simple illustration about the model.)

Based on the electrical double layer system, the working electrode (cathode) is negatively charged such that metal NPs drop-casted on the electrode is negatively charged. The concentration of the solvated cations decreases as the distance from the surface is increased. When the working electrodes are illuminated by visible light, the photocatalytic hydrogen evolution reaction is readily promoted by the LSPR generated hot-electrons, which break the

equilibrium between the metal surface charge and concentration of the solvated cation in the vicinity of the working electrode (in the diffuse layer). Hence, it requires a “cooling-off” period for cations in the outer layer to diffuse through and migrate towards the working electrode surface until a new equilibrium is reached. Therefore, a gradual increase in the photocurrent is observed as a result of the time-delay in reaching the equilibrium period.

Apparent quantum efficiency calculations of AT-layer under different wavelengths:

The AQE was measured in the same conditions as those of a typical EC-LSPR measurement, where a solar simulator (1 sun, AM 1.5G, 100 mW cm⁻²) was used to irradiate the working electrode at three different wavelength ranges of 400-500 nm, 500-600 nm and 600-700 nm. The numbers of photons were calculated from the irradiation powers in each wavelength region measured by a light metre at the corresponding wavelengths. The AQE can be calculated by using the equation:

$$AQE(\%) = \frac{\text{Number of evolved hydrogen molecules} \times 2}{\text{Number of incident photons}} \times 100\%$$

A typical calculation of QE is shown below at a wavelength range of 500-600 nm as an example:

Under an applied potential of -0.5V vs Ag/AgCl, the AT-layer catalyst gives photocurrent in which the amount of hydrogen generated is 0.36 μmol/h, (equivalent to 2.168 × 10¹⁷ hydrogen molecules per hour).

For every 1 hour of reaction,

the energy of light irradiation: $W = P \times t$

Within the wavelength range of 500-600 nm, the light irradiation power is measured to be

$P = 1.1 \text{ mW}$

Therefore the energy $W = 0.00110 \times 3600 = 3.96 \text{ J}$, which contains the photon (550 nm) number of 1.096×10^{19} .

$AQE(\%) = (2 \times 2.168 \times 10^{17}) / (1.096 \times 10^{19}) = 4.0\%$

Table S5. The corresponding apparent quantum efficiencies (AQE) at different wavelength ranges under the same conditions at an applied potential of -0.5 V vs Ag/AgCl of the AT-layer catalyst.

Wavelength/ nm	400-500	500-600	600-700
AQE	2.5%	4.0%	0.9%

Apart from the quantum efficiency, we have also calculated the solar to hydrogen (STH) efficiency:

$$STH = \frac{\text{Output energy as } H_2}{\text{Energy of incident solar light}} = \frac{r_{H_2} \times \Delta G}{P_{sun} \times S}$$

Where r_{H_2} is the rate of hydrogen production, ΔG is the gain in Gibbs energy of 237 kJ mol⁻¹, P_{sun} is the energy flux of the sunlight and S is the area of the working electrode. Considering the ASTM-G173 AM 1.5 global tilt, the solar irradiation has an energy flux of 100 mW cm⁻². For a typical EC-LSPR analysis under an applied potential of -1.2V, the AT-layer gives an STH efficiency of 0.2%.

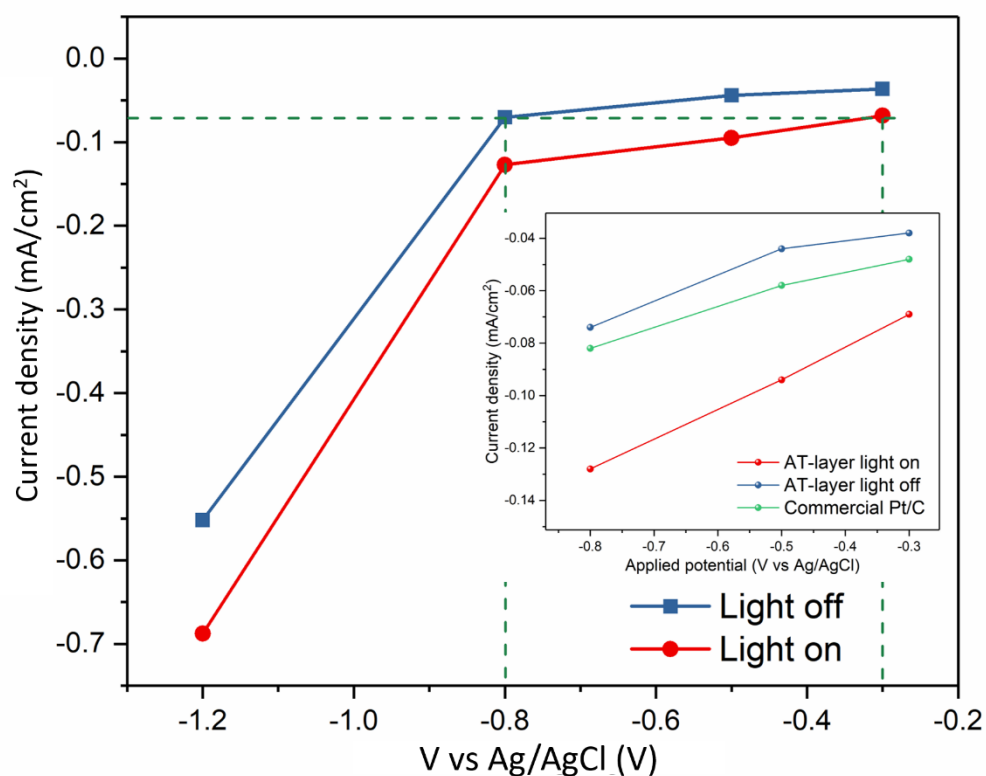


Figure S15. The effect of light illumination on the current density of AT-layer sample at various potentials and the insert shows the comparison between commercial Pt and AT-layer under identical conditions.

Electrolysis at -0.8 V bias without light illumination gives current at 0.07 mA, however, a significantly lower potential at -0.3 V can be applied (160% less power) to maintain the same current when light is utilized, indicative the efficient conversion of light energy to hydrogen.

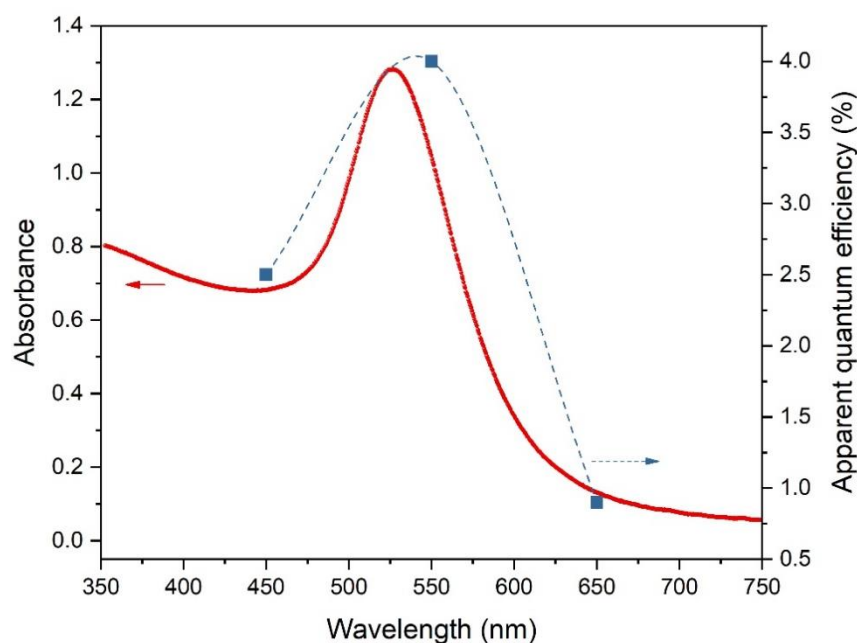


Figure S16. Apparent quantum efficiency (AQE) action spectrum of the AT-layer core-shell electrodes and the corresponding absorption spectra of the AT-layer Au-Ag core-shell nanoparticles.

Although the number of AQE points measured is limited, it can still be clearly observed from Figure S16 that the trend of the spectra profile (in terms of apparent quantum efficiency) is matching with the absorption spectra of AT-layer nanoparticles in general. This sheds light on the fact that the hydrogen generated in the reaction is as a result of photocatalysis and hence, the enhancement in the photocatalytic hydrogen evolution rate can be attributed to the plasmon resonance of the Au-Ag core-shell nanoparticles.

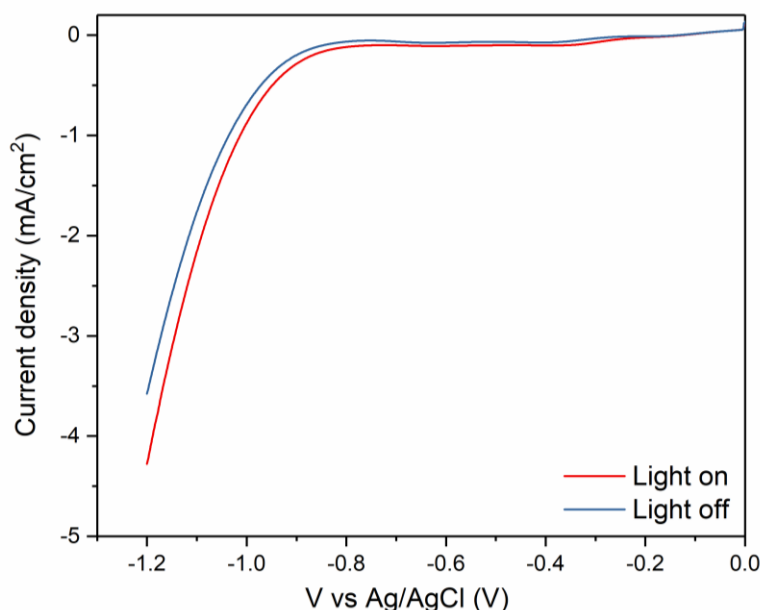


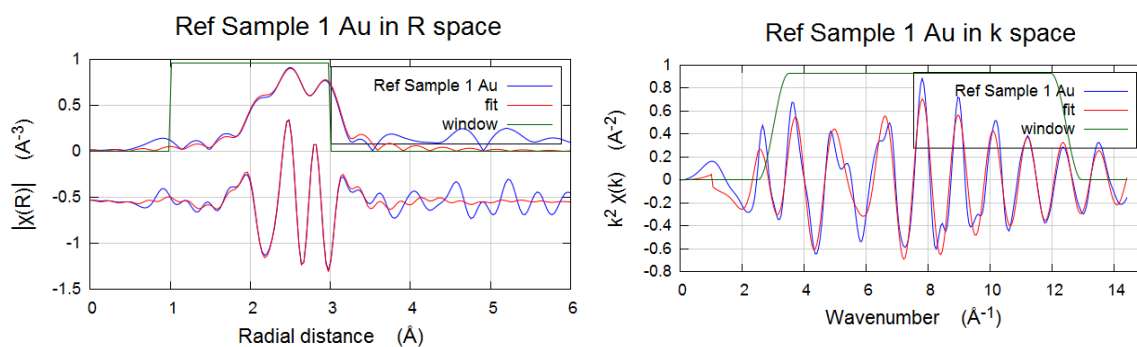
Figure S17. Linear sweep voltammetry (LSV) curves of the AT-layer Au-Ag core-shell NPs in 0.5 M of Na_2SO_4 electrolyte with/without visible light illuminated ($\lambda > 420$ nm) on the working electrode. The scan rate is 1mV/s.

The transient photocurrent response of AT-layer Au-Ag core-shell NPs was measured using continuously linear sweep voltammetry (LSV) under on/off visible light illumination with a typical three electrode system. A solution of 0.5 M Na_2SO_4 (pH 6.5) was used as electrolyte without any addition of sacrificial reagents, which was purged continuously in flowing N_2 to remove O_2 prior to the start of reaction. The AT-layer core-shell NPs was used as a cathode catalyst (working electrode) with a metal loading of 1.2 mg/cm^2 . The scan rate is 1mV/s.

In Figure S17, we can see that the current density under visible light illumination is generally more negative than the light-off condition at the whole potential range (0 V-1.2 V vs Ag/AgCl). In other words, with the aid of LSPR generated hot-electrons under light illuminations, less electrical energy is required to promote the HER reaction, showing the effective conversion of the light energy to hydrogen by using AT-layer Au-Ag core-shell nanoparticles.

9. Extended X-ray absorption fine structure (EXAFS).

The chemical states of Ag and Au local structures in the metallic core-shell NPs were probed by using the extended X-ray absorption fine structure (EXAFS) technique. The Ag K-edge and Au L₃-edge EXAFS measurements were all performed at National Synchrotron Radiation Research Center, Taiwan. The energy resolution ($\Delta E/E$) was 2×10^{-4} . A Si (111) Double Crystal Monochromator (DCM) was used to scan the photon energy. The EXAFS spectra were measured in the fluorescence mode using a Lytle fluorescence detector for all metal samples. The demeter software package (ATHENA & ARTEMIS) was used to analyze the EXAFS data to obtain the local structural parameters of Ag and Au respectively [21]. The amplitude reduction factor of the Ag and Au was obtained from the respective metallic foil, which was used as a fixed input parameter for subsequent analysis. Several constraints were also applied to the fitting parameters to exclude unphysical results.

Au foilAu L_3 edge

k-range: 3-12.5, R-range: 1-3

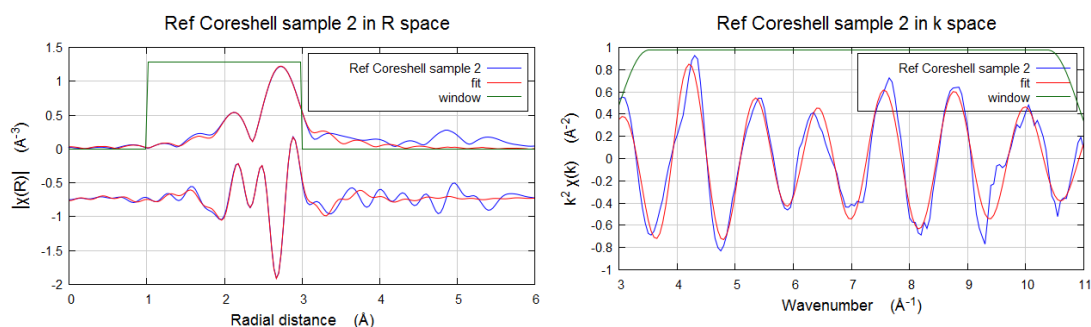
R-factor: 0.4%

Energy difference: 4.2 (4) eV

Amp: 0.85

Scattering Path	Bond length [\AA]	Coordination number	Debye-Waller factor
Au-Au	2.86 (1)	12	0.008 (1)

Figure S18. Least square fitting for the k^3 -weighted EXAFS spectra for the Au foil. Amplitude reduction factor is derived from this spectrum which is used as a fixed parameter for subsequent fittings for the core-shell samples. Both R-space and k-space fitting profile is provided.

Ag foil

Ag K edge

k-range: 3-10.9, R-range: 1-3

R-factor: 0.5%

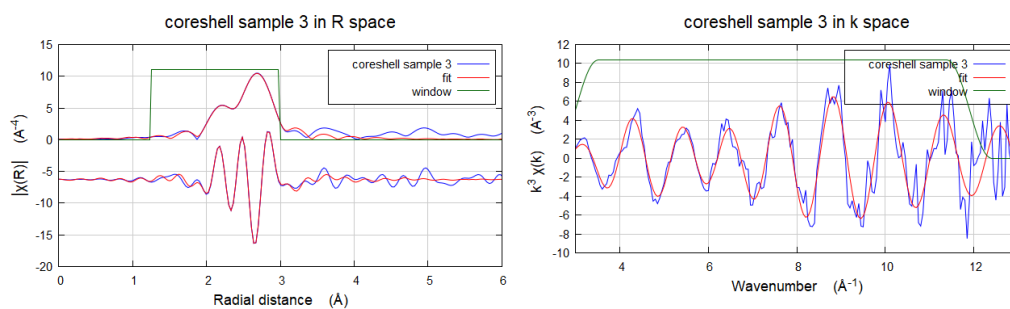
Energy difference: 2.6 (4) eV

Amp: 0.7

Scattering Path	Bond length [\AA]	Coordination number	Debye-Waller factor
Ag-Ag	2.89 (1)	12	0.010 (1)

Figure S19. Least square fitting for the k^3 -weighted EXAFS spectra for the Ag foil. Amplitude reduction factor is derived from this spectrum which is used as a fixed parameter for subsequent fittings for the core-shell samples. Both R-space and k-space fitting profile is provided.

TH-layer Au-Ag core-shell nanoparticle



Ag K edge

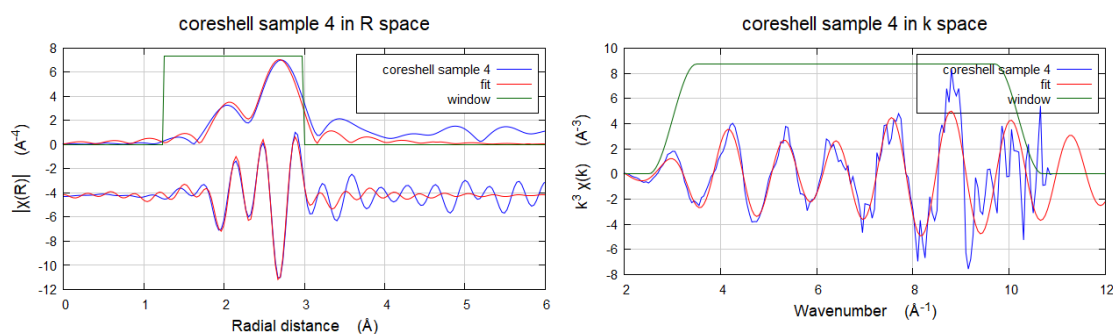
k-range: 3-11.9, R-range: 1.25-3

R-factor: 0.5%

Energy difference: 4.1 eV

Scattering Path	Bond length [Å]	Coordination number	Debye-Waller factor
Ag-Ag	2.87 (1)	11.4 (4)	0.009
Ag-Au	2.90 (3)	1.1 (4)	0.003

Figure S20. Least square fitting for the k^3 -weighted EXAFS spectra (Ag K edge) for the TH-layer Au-Ag core-shell nanoparticles.

IN-layer Au-Ag core-shell nanoparticle

Ag K edge

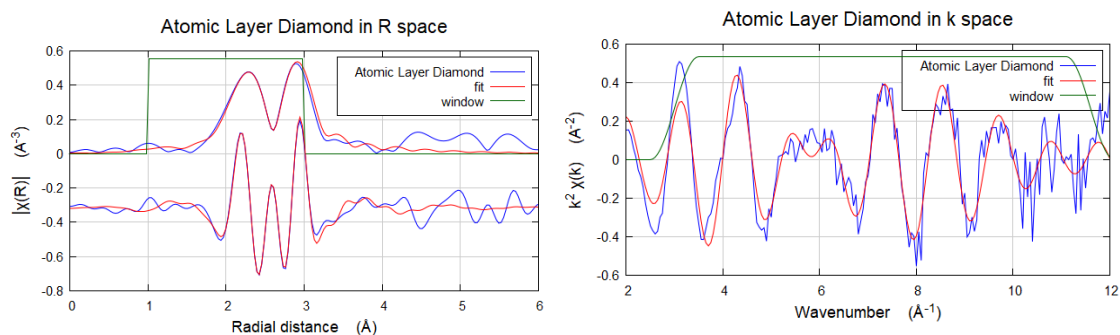
k-range: 3-9.8, R-range: 1.25-3

R-factor: 0.9%

Energy difference: -0.5 eV

Scattering Path	Bond length [\AA]	Coordination number	Debye-Waller factor
Ag-Ag	2.86 (1)	11.1 (5)	0.010
Ag-Au	2.89 (3)	1.8 (7)	0.010

Figure S21. Least square fitting for the k^3 -weighted EXAFS spectra (Ag K edge) for the IN-layer Au-Ag core-shell nanoparticles.

AT- layer Au-Ag core-shell nanoparticle

Ag K edge

Amplitude reduction factor: 0.7

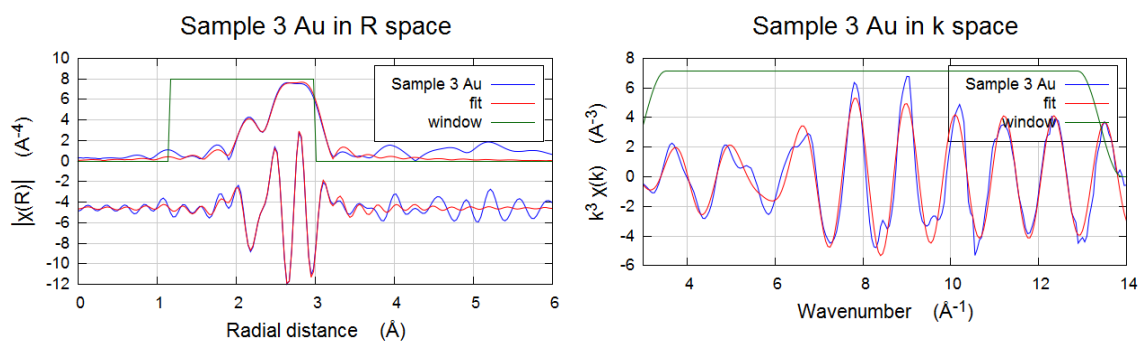
k-range: 3-11.6; R-range: 1-3

R-factor: 1.4%

Energy difference: 3.9 eV

Scattering Path	Bond length [\AA]	Coordination number	Debye-Waller factor
Ag-Ag	2.88 (2)	2.1 (3)	0.005
Ag-Au	2.89 (2)	5.7 (4)	0.005

Figure S22. Least square fitting for the k^3 -weighted EXAFS spectra (Ag K edge) for the AT-layer Au-Ag core-shell nanoparticles.

TH-layer Au-Ag core-shell nanoparticle

Au L_3 edge

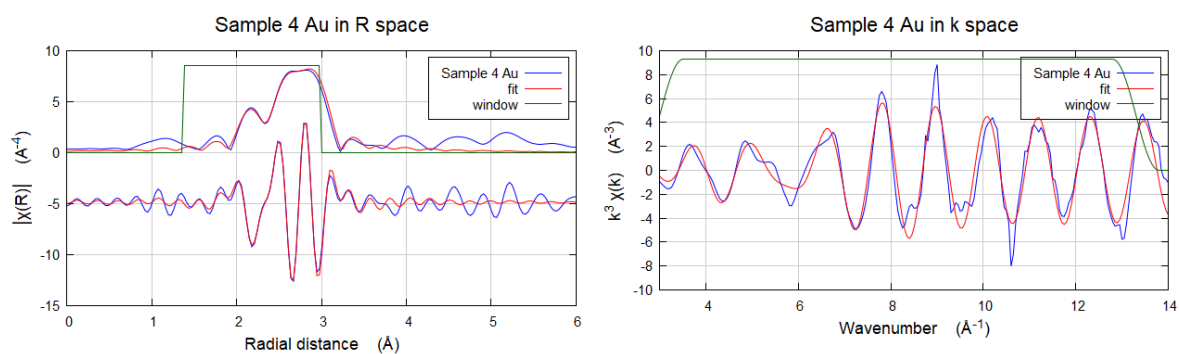
k-range: 3-13.4, R-range: 1.15-3

R-factor: 0.5%

Energy difference: 4.7 (8) eV

Scattering Path	Bond length [\AA]	Coordination number	Debye-Waller factor
Au-Au	2.86 (1)	10.7 (7)	0.008 (1)
Au-Ag	2.87 (1)	0.5 (0.6)	0.009 (5)

Figure S23. Least square fitting for the k^3 -weighted EXAFS spectra (Au L_3 edge) for the TH-layer Au-Ag core-shell nanoparticles.

IN-layer Au-Ag core-shell nanoparticle

Au L_3 edge

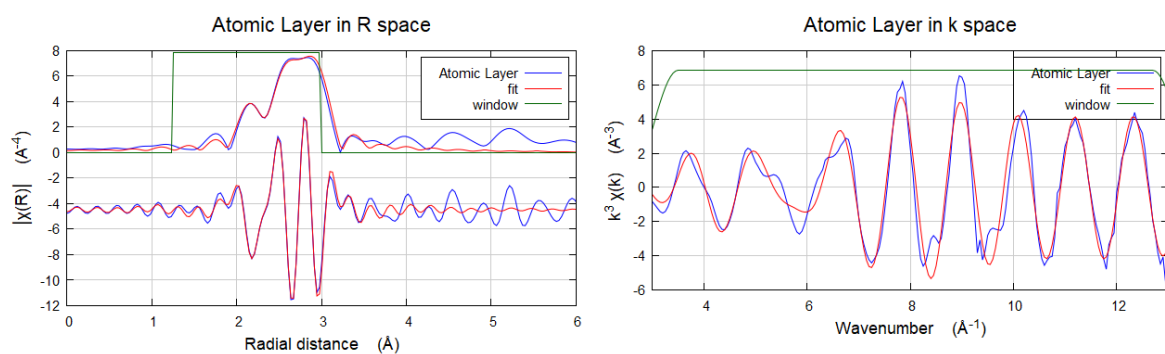
k-range: 3-13.3, R-range: 1.35-3

R-factor: 0.5%

Energy difference: 5.4 (0.6) eV

Scattering Path	Bond length [\AA]	Coordination number	Debye-Waller factor
Au-Au	2.87 (1)	10.6 (0.4)	0.008
Au-Ag	2.89 (4)	0.9 (0.4)	0.011

Figure S24. Least square fitting for the k^3 -weighted EXAFS spectra (Au L_3 edge) for the IN-layer Au-Ag core-shell nanoparticles.

AT-layer Au-Ag core-shell nanoparticle

Au L_3 edge

k-range: 3-13.2, R-range: 1.25-3

R-factor: 0.6%

Energy difference: 5.8 (7) eV

Scattering Path	Bond length [\AA]	Coordination number	Debye-Waller factor
Au-Au	2.87 (1)	10.0 (4)	0.008
Au-Ag	2.92 (1)	1.2 (5)	0.014

Figure S25. Least square fitting for the k^3 -weighted EXAFS spectra (Au L_3 edge) for the AT-layer Au-Ag core-shell nanoparticles.

10. Discrete dipole approximation (DDA).

The discrete dipole approximation (DDA) is an effective approach developed for calculating the far-field and near-field properties of metallic nanoparticles. In this theoretical model, the nanostructures are described as a cubic array lattice of electric dipoles (N -point dipoles). The polarizability and position vector of each dipole are specified as \mathbf{P}_i and \mathbf{r}_i , where $i = 1, 2, \dots, N$, respectively. When the nanostructure is excited by a polarized incident electromagnetic wave, the polarization induced at each dipole that represents a discrete volume of material can be written as

$$\mathbf{P}_i = \alpha_i \cdot \mathbf{E}_{loc,i}(\mathbf{r}_i) \quad (1)$$

where $\mathbf{E}_{loc,i}(\mathbf{r}_i)$ represents the local field, defined as the sum of the field radiated from all other $N-1$ dipoles, $\mathbf{E}_{dip,i}(\mathbf{r}_i)$, and the incident radiation field, $\mathbf{E}_{inc,i}(\mathbf{r}_i)$. $\mathbf{E}_{loc,i}(\mathbf{r}_i)$ can be expressed using the dipole-dipole interaction matrix \mathbf{A} , represented by

$$\mathbf{A}_{ij} \cdot \mathbf{P}_j = \frac{\exp(ikr_{ij})}{r_{ij}^3} \left\{ k^2 \mathbf{r}_{ij} \times (\mathbf{r}_{ij} \times \mathbf{P}_j) + \frac{1 - ikr_{ij}}{r_{ij}^2} \times [r_{ij}^2 \mathbf{P}_j - 3\mathbf{r}_{ij}(\mathbf{r}_{ij} \cdot \mathbf{P}_j)] \right\} \quad (2)$$

$(j = 1, 2, \dots, N, j \neq i)$

where \mathbf{r}_{ij} and r_{ij} coordinates are defined as $\mathbf{r}_i - \mathbf{r}_j$ and $|\mathbf{r}_i - \mathbf{r}_j|$ respectively, and correspond to the dipole-dipole distance. Assuming $\mathbf{E}_{inc,i}(\mathbf{r}_i)$ to be a plane wave, the local field can be written as

$$\mathbf{E}_{loc,i}(\mathbf{r}_i) = \mathbf{E}_0 \exp(i\mathbf{k} \cdot \mathbf{r}_i) - \sum_{j \neq i} \mathbf{A}_{ij} \cdot \mathbf{P}_j \quad (3)$$

where \mathbf{k} and \mathbf{E}_0 are the wavevector and amplitude of the incident radiation. Replacing the Eq. (2) into the Eq. (3) allows the Eq. (3) in the matrix form

$$\mathbf{E} = \mathbf{A}' \cdot \mathbf{P} \quad (4)$$

where \mathbf{A}' is a matrix derived from equation (2). \mathbf{P} and \mathbf{E} are $3N$ -dimensional vectors with components \mathbf{P}_i and $\mathbf{E}_{loc,i}(\mathbf{r}_i)$, respectively. Then, solving the $3N$ complex linear equations, one can obtain the local fields \mathbf{E} as well as the extinction and absorption cross sections, given by

$$C_{ext} = \frac{4\pi k}{|\mathbf{E}_0|^2} \sum_{i=1}^N \text{Im}(\mathbf{E}_{loc,i}^* \cdot \mathbf{P}_i) \quad (5)$$

$$C_{abs} = \frac{4\pi k}{|\mathbf{E}_0|^2} \sum_{i=1}^N \left\{ \text{Im}[\mathbf{P}_i \cdot (\alpha_i^{-1})^* \mathbf{P}_i^*] - \frac{2k^3}{3} |\mathbf{P}_i|^2 \right\} \quad (6)$$

where Im denotes the imaginary part of the expression in the brackets, and $*$ the usual complex conjugate. Finally, the scattering cross section can be determined by

$$C_{sca} = C_{ext} - C_{abs} \quad (7)$$

In this work, equation (4) was solved using the free code DDSCAT 7.3 implemented by Draine and Flatau [22–26]. The extinction efficiency factor, the absorption efficiency factor, and the scattering efficiency factor are expressed as

$$Q_{sca} = \frac{C_{sca}}{\pi a_{eff}^2}, Q_{ext} = \frac{C_{ext}}{\pi a_{eff}^2} \text{ and } Q_{abs} = \frac{C_{abs}}{\pi a_{eff}^2},$$

where a_{eff} is the effective radius defined for the target volume as $a_{eff} = (3V/4\pi)^{1/3}$. The E-field distributions for Au-Ag core-shell nanoparticles, with a fixed diameter gold core of 26.6 nm were calculated using this approach. Based on the experimental evidence, the Ag thickness as defined as 1, 3 and 5 nm. In the case shell thickness of 1 nm, the E-field for different Ag-Au compositions (increasing Ag content from 0-100%) were also calculated. In these calculations, a range from 450 to 550 nm were employed as the wavelength of the incident electromagnetic wave and the polarization direction for sphere and shell along the y-axis. For the cubic grid, we employed a spacing of 0.5 nm for all nanostructures. The medium refraction index was 1.0 (air) in all cases. The near-fields were described by a grid of 4.0×10^4 points on the yz plane, the dielectric constants for Au, Ag, and Ag-Au alloys were obtained from the literature [27,28]. The DDA Convert Tool [29] was used to convert a non-standard geometry (shell and rattle), generated by Blender 3D editor [30].

Table S6. Optimized structures of Au-Ag core-shell nanoparticles with fixed diameter gold core of 26 nm and fixed shell thickness with 0.8 nm composed of different Ag-Au (increasing Ag content from 0-100%). The response of induced electric field enhancement $|E^2|/|E_0^2|$ of the nanoparticles with different shell compositions as a function of wavelength can be seen.

λ/nm	100 Au	30/70	40/60	70/30	80/20	100 Ag
		Ag/Au	Ag/Au	Ag/Au	Ag/Au	
450	13.35	14.95	15.78	18.29	19.21	19.41
460	13.41	15.62	16.50	18.79	19.35	25.23
470	13.55	16.46	17.33	20.10	22.00	29.35
480	14.01	17.74	18.90	23.85	26.64	33.11
490	15.83	21.41	23.55	30.49	33.77	39.69
500	19.88	28.48	31.20	38.88	41.84	46.66
510	25.22	36.50	38.97	45.03	47.04	49.99
520	29.94	42.21	43.78	47.44	48.51	49.49
530	32.81	44.61	45.41	47.51	48.07	48.40
540	33.73	44.80	45.29	46.87	47.36	48.19
550	33.31	44.12	44.57	46.20	46.84	48.15

References:

- [1] J. Turkevich, P.C. Stevenson, J. Hillier, A study of the nucleation and growth processes in the synthesis of colloidal gold, *Discuss. Faraday Soc.* 11 (1951) 55–75.
<https://doi.org/10.1039/DF9511100055>.
- [2] A.K. Samal, L. Polavarapu, S. Rodal-Cedeira, L.M. Liz-Marzán, J. Pérez-Juste, I. Pastoriza-Santos, Size tunable Au@Ag core-shell nanoparticles: Synthesis and surface-enhanced raman scattering properties, *Langmuir*. 29 (2013) 15076–15082.
<https://doi.org/10.1021/la403707j>.
- [3] J. Zeng, Y. Zheng, M. Rycenga, J. Tao, Z.Y. Li, Q. Zhang, Y. Zhu, Y. Xia, Controlling the shapes of silver nanocrystals with different capping agents, *J. Am. Chem. Soc.* 132 (2010) 8552–8553. <https://doi.org/10.1021/ja103655f>.
- [4] P. Felfer, T. Li, K. Eder, H. Galinski, A.P. Magyar, D.C. Bell, G.D.W. Smith, N. Kruse, S.P. Ringer, J.M. Cairney, New approaches to nanoparticle sample fabrication for atom probe tomography, *Ultramicroscopy*. 159 (2015) 413–419.
<https://doi.org/10.1016/j.ultramic.2015.04.014>.
- [5] M. Kociak, O. Stéphan, Mapping plasmons at the nanometer scale in an electron microscope, *Chem. Soc. Rev.* 43 (2014) 3865–3883.
<https://doi.org/10.1039/c3cs60478k>.
- [6] L.I. Ibarra-Rodriguez, A.M. Huerta-Flores, J.M. Mora-Hernandez, L.M. Torres-Martínez, Photocatalytic evolution of H₂ over visible-light active LaMO₃ (M: Co, Mn, Fe) perovskite materials: Roles of oxygenated species in catalytic performance, *J. Phys. Chem. Solids*. 136 (2020) 109189. <https://doi.org/10.1016/j.jpcs.2019.109189>.
- [7] O.A. Carrasco-Jaim, J.M. Mora-Hernandez, L.M. Torres-Martínez, E. Moctezuma, A comparative study on the photocatalytic hydrogen production of ATiO₃ (A = Zn, Cd and Pb) perovskites and their photoelectrochemical properties, *J. Photochem. Photobiol. A Chem.* 371 (2019) 98–108.
<https://doi.org/10.1016/j.jphotochem.2018.11.004>.
- [8] H. He, J. Cao, M. Guo, H. Lin, J. Zhang, Y. Chen, S. Chen, Distinctive ternary CdS/Ni₂P/g-C₃N₄ composite for overall water splitting: Ni₂P accelerating separation of photocarriers, *Appl. Catal. B Environ.* 249 (2019) 246–256.
<https://doi.org/10.1016/j.apcatb.2019.02.055>.
- [9] Y. Zhong, Y. Wu, B. Chang, Z. Ai, K. Zhang, Y. Shao, L. Zhang, X. Hao, A CoP/CdS/WS₂ p-n-n tandem heterostructure: A novel photocatalyst for hydrogen evolution without using sacrificial agents, *J. Mater. Chem. A*. 7 (2019) 14638–14645.
<https://doi.org/10.1039/c9ta03721g>.
- [10] W. Liu, L. Cao, W. Cheng, Y. Cao, X. Liu, W. Zhang, X. Mou, L. Jin, X. Zheng, W. Che, Q. Liu, T. Yao, Single-Site Active Cobalt-Based Photocatalyst with a Long Carrier Lifetime for Spontaneous Overall Water Splitting *Angewandte, Angew.* 129 (2017) 9440–9445. <https://doi.org/10.1002/ange.201704358>.
- [11] K. Han, T. Kreuger, B. Mei, G. Mul, Transient Behavior of Ni@NiO_x Functionalized SrTiO₃ in Overall Water Splitting, *ACS Catal.* 7 (2017) 1610–1614.
<https://doi.org/10.1021/acscatal.6b03662>.
- [12] D. Zheng, X. Cao, X. Wang, Precise Formation of a Hollow Carbon Nitride Structure with a Janus Surface To Promote Water Splitting by Photoredox Catalysis, *Angew. Chemie - Int. Ed.* 128 (2016) 11684–11688. <https://doi.org/10.1002/ange.201606102>.
- [13] W. Fang, J. Liu, D. Yang, Z. Wei, Z. Jiang, W. Shangguan, Effect of Surface Self-Heterojunction Existed in Bi₂Y_{1-x}VO₄ on Photocatalytic Overall Water Splitting, *ACS Sustain. Chem. Eng.* 5 (2017) 6578–6584.
<https://doi.org/10.1021/acssuschemeng.7b00808>.

- [14] E. Article, G. Zhang, Z. Lan, L. Lin, S. Lin, X. Wang, Overall water splitting by Pt/g-C₃N₄ photocatalysts without using sacrificial agents, *Chem. Sci.* 7 (2016) 3062–3066. <https://doi.org/10.1039/c5sc04572j>.
- [15] W. Che, W. Cheng, T. Yao, F. Tang, W. Liu, H. Su, Y. Huang, Q. Liu, J. Liu, F. Hu, Z. Pan, Z. Sun, S. Wei, Fast Photoelectron Transfer in (Cring)–C₃N₄ Plane Heterostructural Nanosheets for Overall Water Splitting, *J. Am. Chem. Soc.* 139 (2017) 3021–3026. <https://doi.org/10.1021/jacs.6b11878>.
- [16] Z. Pan, Y. Zheng, F. Guo, P. Niu, X. Wang, Decorating CoP and Pt Nanoparticles on Graphitic Carbon Nitride Nanosheets to Promote Overall Water Splitting by Conjugated Polymers, *ChemSusChem*. 9 (2016) 1–5. <https://doi.org/10.1002/cssc.201600850>.
- [17] J. Yan, H. Wu, H. Chen, Y. Zhang, F. Zhang, S. Frank, Fabrication of TiO₂/C₃N₄ heterostructure for enhanced photocatalytic Z-scheme overall water splitting, *Applied Catal. B, Environ.* 191 (2016) 130–137. <https://doi.org/10.1016/j.apcatb.2016.03.026>.
- [18] N. V. Ryzhkov, V. Y. Yurova, S. A. Ulasevich, E. V. Skorb, Photoelectrochemical photocurrent switching effect on a pristine anodized Ti/TiO₂ system as a platform for chemical logic devices, *RSC Adv.* 10 (2020) 12355–12359. <https://doi.org/10.1039/D0RA00205D>.
- [19] X. Huang, M. A. El-Sayed, Gold nanoparticles: Optical properties and implementations in cancer diagnosis and photothermal therapy, *J. Adv. Res.* 1 (2010) 13–28. <https://doi.org/10.1016/j.jare.2010.02.002>.
- [20] E. Partheniades, Cohesive Sediments in Open Channels, in: Butterworth-Heinemann, 2009: p. 384. <https://doi.org/https://doi.org/10.1016/B978-1-85617-556-2.X0001-7>.
- [21] B. Ravel, M. Newville, ATHENA, ARTEMIS, HEPHAESTUS: Data analysis for X-ray absorption spectroscopy using IFEFFIT, in: *J. Synchrotron Radiat.*, International Union of Crystallography, 2005: pp. 537–541. <https://doi.org/10.1107/S0909049505012719>.
- [22] M.J. Collinge, B.T. Draine, Discrete-dipole approximation with polarizabilities that account for both finite wavelength and target geometry, *J. Opt. Soc. Am. A.* 21 (2004) 2023–2028.
- [23] J. Draine, B. T. & Goodman, Beyond Clausius-Mossotti - Wave propagation on a polarizable point lattice and the discrete dipole approximation, *Astrophys. Journal, Part 1* (ISSN 0004-637X). 405 (1993) 685–697.
- [24] J.J. Goodman, B.T. Draine, P.J. Flatau, Application of fast-Fourier-transform techniques to the discrete-dipole approximation, *Opt. Lett.* 16 (1991) 1198–1200.
- [25] B.T. Draine, P.J. Flatau, Discrete-Dipole Approximation For Scattering Calculations, *J. Opt. Soc. Am. A.* 11 (1994) 1491–1499. <https://doi.org/10.1364/josaa.11.001491>.
- [26] B. T. Draine, P. J. Flatau, User guide to the discrete dipole approximation code DDSCAT 7.3, (n.d.). <http://arxiv.org/abs/1305.6497>.
- [27] P. B. Johnson and R. W. Christy, Optical Constant of the Nobel Metals, *Phys. L Re View B.* 6 (1972) 4370–4379.
- [28] D. Rioux, S. Vallières, S. Besner, P. Muñoz, E. Mazur, M. Meunier, An analytic model for the dielectric function of Au, Ag, and their Alloys, *Adv. Opt. Mater.* 2 (2014) 176–182. <https://doi.org/10.1002/adom.201300457>.
- [29] J. Feser, A. N. Sobh, DDSCAT Convert: A Target Generation Tool, (n.d.). <https://nanohub.org/resources/ddaconvert>.
- [30] Blender Online Community, Blender - a 3D modelling and rendering package, (n.d.). <http://www.blender.org/>.